We are IntechOpen, the world's leading publisher of Open Access books Built by scientists, for scientists

4,800
Open access books available

122,000
International authors and editors

135M
Downloads

Our authors are among the

154
Countries delivered to

TOP 1%
most cited scientists

12.2%
Contributors from top 500 universities

WEB OF SCIENCE™

Selection of our books indexed in the Book Citation Index in Web of Science™ Core Collection (BKCI)

Interested in publishing with us?
Contact book.department@intechopen.com

Numbers displayed above are based on latest data collected.
For more information visit www.intechopen.com

9

Controller Design for Synchronous Reluctance Motor Drive Systems with Direct Torque Control

Tian-Hua Liu
Department of Electrical Engineering,
National Taiwan University of Science and Technolog
Taiwan

1. Introduction

A. Background

The synchronous reluctance motor (SynRM) has many advantages over other ac motors. For example, its structure is simple and rugged. In addition, its rotor does not have any winding or magnetic material. Prior to twenty years ago, the SynRM was regarded as inferior to other types of ac motors due to its lower average torque and larger torque pulsation. Recently, many researchers have proposed several methods to improve the performance of the motor and drive system [1]-[3]. In fact, the SynRM has been shown to be suitable for ac drive systems for several reasons. For example, it is not necessary to compute the slip of the SynRM as it is with the induction motor. As a result, there is no parameter sensitivity problem. In addition, it does not require any permanent magnetic material as the permanent synchronous motor does.

The sensorless drive is becoming more and more popular for synchronous reluctance motors. The major reason is that the sensorless drive can save space and reduce cost. Generally speaking, there are two major methods to achieve a sensorless drive system: vector control and direct torque control. Although most researchers focus on vector control for a sensorless synchronous reluctance drive [4]-[12], direct torque control is simpler. By using direct torque control, the plane of the voltage vectors is divided into six or twelve sectors. Then, an optimal switching strategy is defined for each sector. The purpose of the direct torque control is to restrict the torque error and the stator flux error within given hysteresis bands. After executing hysteresis control, a switching pattern is selected to generate the required torque and flux of the motor. A closed-loop drive system is thus obtained.

Although many papers discuss the direct torque control of induction motors [13]-[15], only a few papers study the direct torque control for synchronous reluctance motors. For example, Consoli et al. proposed a sensorless torque control for synchronous reluctance motor drives [16]. In this published paper, however, only a PI controller was used. As a result, the transient responses and load disturbance responses were not satisfactory. To solve the problem, in this chapter, an adaptive backstepping controller and a model-reference adaptive controller are proposed for a SynRM direct torque control system. By using the

proposed controllers, the transient responses and load disturbance rejection capability are obviously improved. In addition, the proposed system has excellent tracking ability. As to the authors best knowledge, this is the first time that the adaptive backstepping controller and model reference adaptive controller have been used in the direct torque control of synchronous reluctance motor drives. Several experimental results validate the theoretical analysis.

B. Literature Review

Several researchers have studied synchronous reluctance motors. These researchers use different methods to improve the performance of the synchronous reluctance motor drive system. The major categories include the following five methods:

1. Design and manufacture of the synchronous reluctance motor

The most effective way to improve the performance of the synchronous reluctance motor is to design the structure of the motor, which includes the rotor configuration, the windings, and the material. Miller et al. proposed a new configuration to design the rotor configuration. By using the proposed method, a maximum L_d / L_q ratio to reach high power factor, high torque, and low torque pulsations was achieved [17]. In addition, Vagati et al. used the optimization technique to design a rotor of the synchronous reluctance motor. By applying the finite element method, a high performance, low torque pulsation synchronous reluctance motor has been designed [18]. Generally speaking, the design and manufacture of the synchronous reluctance motor require a lot of experience and knowledge.

2. Development of Mathematical Model for the synchronous reluctance motor

The mathematical model description is required for analyzing the characteristics of the motor and for designing controllers for the closed-loop drive system. Generally speaking, the core loss and saturation effect are not included in the mathematical model. However, recently, several researchers have considered the influence of the core loss and saturation. For example, Uezato et al. derived a mathematical model for a synchronous reluctance motor including stator iron loss [19]. Sturtzer et al. proposed a torque equation for synchronous reluctance motors considering saturation effect [2]. Stumberger discussed a parameter measuring method of linear synchronous reluctance motors by using current, rotor position, flux linkages, and friction force [20]. Ichikawa et al. proposed a rotor estimating technique using an on-line parameter identification method taking into account magnetic saturation [5].

3. Controller Design

As we know, the controller design can effectively improve the transient responses, load disturbance responses, and tracking responses for a closed-loop drive system. The PI controller is a very popular controller, which is easy to design and implement. Unfortunately, it is impossible to obtain fast transient responses and good load disturbance responses by using a PI controller. To solve the difficulty, several advanced controllers have been developed. For example, Chiang et al. proposed a sliding mode speed controller with a grey prediction compensator to eliminate chattering and reduce steady-state error [21]. Lin et al. used an adaptive recurrent fuzzy neural network controller for synchronous reluctance motor drives [22]. Morimoto proposed a low resolution encoder to achieve a high performance closed-loop drive system [7].

4. Rotor estimating technique

The sensorless synchronous reluctance drive system provides several advantages. For example, sensorless drive systems do not require an encoder, which increases cost,

generates noise, and requires space. As a result, the sensorless drive systems can reduce costs and improve reliability. Several researchers have studied the rotor estimating technique to realize a sensorless drive. For example, Lin et al. used a current-slope to estimate the rotor position and rotor speed [4]. Platt et al. implemented a sensorless vector controller for a synchronous reluctance motor [9]. Kang et al. combined the flux-linkage estimating method and the high-frequency injecting current method to achieve a sensorless rotor position/ speed drive system [23]. Ichikawa presented an extended EMF model and initial position estimation for synchronous motors [10].

5. Switching strategy of the inverter for synchronous reluctance motor

Some researchers proposed the switching strategies of the inverter for synchronous reluctance motors. For example, Shi and Toliyat proposed a vector control of a five-phase synchronous reluctance motor with space vector pulse width modulation for minimum switching losses [24].

Recently, many researchers have created new research topics for synchronous reluctance motor drives. For example, Gao and Chau present the occurrence of Hopf bifurcation and chaos in practical synchronous reluctance motor drive systems [25]. Bianchi, Bolognani, Bon, and Pre propose a torque harmonic compensation method for a synchronous reluctance motor [26]. Iqbal analyzes dynamic performance of a vector-controlled five-phase synchronous reluctance motor drive by using an experimental investigation [27]. Morales and Pacas design an encoderless predictive direct torque control for synchronous reluctance machines at very low and zero speed [28]. Park, Kalev, and Hofmann propose a control algorithm of high-speed solid-rotor synchronous reluctance motor/ generator for flywheel-based uniterruptible power supplies [29]. Liu, Lin, and Yang propose a nonlinear controller for a synchronous reluctance drive with reduced switching frequency [30]. Ichikawa, Tomita, Doki, and Okuma present sensorless control of synchronous reluctance motors based on extended EMF models considering magnetic saturation with online parameter identification [31].

2. The synchronous reluctance motor

In the section, the synchronous reluctance motor is described. The details are discussed as follows.

2.1 Structure and characteristics

Synchronous reluctance motors have been used as a viable alternative to induction and switched reluctance motors in medium-performance drive applications, such as: pumps, high-efficiency fans, and light road vehicles. Recently, axially laminated rotor motors have been developed to reach high power factor and high torque density. The synchronous reluctance motor has many advantages. For example, the synchronous reluctance motor does not have any rotor copper loss like the induction motor has. In addition, the synchronous reluctance motor has a smaller torque pulsation as compared to the switched reluctance motor.

2.2 Dynamic mathematical model

In synchronous d-q reference frame, the voltage equations of the synchronous reluctance motor can be described as

$$v_{qs} = r_s i_{qs} + p\lambda_{qs} + \omega_r \lambda_{ds} \tag{1}$$

$$v_{ds} = r_s i_{ds} + p\lambda_{ds} - \omega_r \lambda_{qs} \tag{2}$$

where v_{qs} and v_{ds} are the q-axis and the d-axis voltages, r_s is the stator resistance, i_{qs} is the q-axis equivalent current, i_{ds} is the d-axis equivalent current, p is the differential operator, λ_{qs} and λ_{ds} are the q-axis and d-axis flux linkages, and ω_r is the motor speed. The flux linkage equations are

$$\lambda_{qs} = (L_{ls} + L_{mq})\ i_{qs} \tag{3}$$

$$\lambda_{ds} = (L_{ls} + L_{md})\ i_{ds} \tag{4}$$

where L_{ls} is the leakage inductance, and L_{mq} and L_{md} are the q- axis and d-axis mutual inductances. The electro-magnetic torque can be expressed as

$$T_e = \frac{3}{2}\ \frac{P_0}{2}\ (L_{md} - L_{mq})\ i_{ds}\ i_{qs} \tag{5}$$

where T_e is the electro-magnetic torque of the motor, and P_0 is the number of poles of the motor. The rotor speed and position of the motor can be expressed as

$$p\,\omega_{rm} = \frac{1}{J}(T_e - T_l - B\,\omega_{rm}) \tag{6}$$

and

$$p\,\theta_{rm} = \omega_{rm} \tag{7}$$

where J is the inertia constant of the motor and load, T_l is the external load torque, B is the viscous frictional coefficient of the motor and load, θ_{rm} is the mechanical rotor position, and ω_{rm} is the mechanical rotor speed. The electrical rotor speed and position are

$$\omega_r = \frac{P_0}{2}\omega_{rm} \tag{8}$$

$$\theta_r = \frac{P_0}{2}\theta_{rm} \tag{9}$$

where ω_r is the electrical rotor speed, and θ_r is the electrical rotor position of the motor.

2.3 Steady-state analysis

When the synchronous reluctance motor is operated in the steady-state condition, the d-q axis currents, i_d and i_q, become constant values. We can then assume $x_q = \omega_e L_{qs}$ and $x_d = \omega_e\ L_{ds}$, and derive the steady-state d-q axis voltages as follows:

$$v_d = r_s i_d - x_q i_q \tag{10}$$

$$v_q = r_s i_q + x_d i_d \tag{11}$$

The stator voltage can be expressed as a vector V_s and shown as follows

$$V_s = v_q - jv_d \tag{12}$$

Now, from equations (10) and (11), we can solve the d-axis current and q-axis current as

$$i_d = \frac{r_s v_d + x_q v_q}{r_s^2 + x_d x_q} \tag{13}$$

and

$$i_q = \frac{r_s v_q - x_d v_d}{r_s^2 + x_d x_q} \tag{14}$$

By substituting equations (13)-(14) into (5), we can obtain the steady-state torque equation as

$$T_e = \frac{3}{2}\frac{P}{2}\frac{1}{\omega_e}\frac{x_d - x_q}{(r_s^2 + x_d x_q)^2}[(r_s x_q v_q^2) - (r_s x_d v_d^2) + (r_s^2 - x_d x_q) v_d v_q] \tag{15}$$

According to (15), when the stator resistance r_s is very small and can be neglected, the torque equation (15) can be simplified as

$$T_e = \frac{3}{2}\frac{P}{2}\frac{1}{\omega_e}\frac{x_d - x_q}{2x_d x_q} V_s^2 \sin(2\delta) \tag{16}$$

The output power is

$$\begin{aligned} P &= T_e \frac{\omega_e}{(\frac{P}{2})} \\ &= \frac{3}{2}\frac{x_d - x_q}{2x_d x_q} V_s^2 \sin(2\delta) \end{aligned} \tag{17}$$

where P is the output power, and δ is the load angle.

3. Direct torque control

3.1 Basic principle

Fig. 1 shows the block diagram of the direct torque control system. The system includes two major loops: the torque-control loop and the flux-control loop. As you can observe, the flux and torque are directly controlled individually. In addition, the current-control loop is not required here. The basic principle of the direct torque control is to bound the torque error and the flux error in hysteresis bands by properly choosing the switching states of the inverter. To achieve this goal, the plan of the voltage vector is divided into six operating

sectors and a suitable switching state is associated with each sector. As a result, when the voltage vector rotates, the switching state can be automatically changed. For practical implementation, the switching procedure is determined by a state selector based on pre-calculated look up tables. The actual stator flux position is obtained by sensing the stator voltages and currents of the motor. Then, the operating sector is selected. The resolution of the sector is 60 degrees for every sector. Although the direct torque is very simple, it shows good dynamic performance in torque regulation and flux regulation. In fact, the two loops on torque and flux can compensate the imperfect field orientation caused by the parameter variations. The disadvantage of the direct torque control is the high frequency ripples of the torque and flux, which may deteriorate the performance of the drive system. In addition, an advanced controller is not easy to apply due to the large torque pulsation of the motor.

In Fig.1, the estimating torque and flux can be obtained by measuring the a-phase and the b-phase voltages and currents. Next, the speed command is compared with the estimating speed to compute the speed error. Then, the speed error is processed by the speed controller to obtain the torque command. On the other hand, the flux command is compared to the estimated flux. Finally, the errors ΔT_e and $\Delta\lambda_s$ go through the hysteresis controllers and the switching table to generate the required switching states. The synchronous reluctance motor rotates and a closed-loop drive system is thus achieved. Due to the limitation of the scope of this paper, the details are not discussed here.

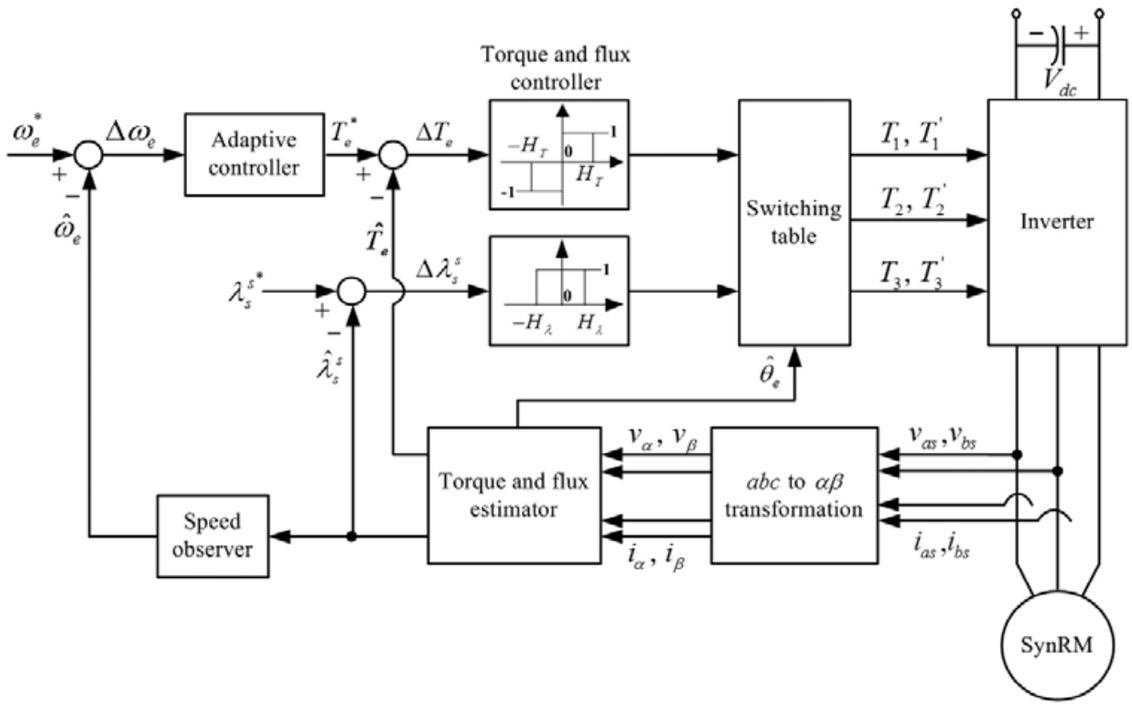

Fig. 1. The block diagram of the direct torque control system

3.2 Controller design

The SynRM is easily saturated due to its lack of permanent magnet material. As a result, it has nonlinear characteristics under a heavy load. To solve the problem, adaptive control algorithms are required. In this paper, two different adaptive controllers are proposed.

A. Adaptive Backstepping Controller

From equation (6), it is not difficult to derive

$$\begin{aligned}\frac{d}{dt}\omega_r &= \frac{1}{J_m}\left[T_e - T_L - B_m\omega_r\right] \\ &= A_1 T_e + A_2 T_L + A_3\omega_r\end{aligned} \tag{18}$$

and

$$A_1 = \frac{1}{J_m} \tag{19}$$

$$A_2 = -\frac{1}{J_m} \tag{20}$$

$$A_3 = -\frac{B_m}{J_m} \tag{21}$$

Where A_1, A_2, A_3 are constant parameters which are related to the motor parameters. In the real world, unfortunately, the parameters of the SynRM can not be precisely measured and are varied by saturated effect or temperature. As a result, a controller designer should consider the problem. In this paper, we proposed two control methods. The first one is an adaptive backstepping controller. In this method, we consider the parameter variations and external load together. Then

$$\frac{d}{dt}\omega_r = A_1 T_e + A_3\omega_r + (A_2 T_L + \Delta A_1 T_e + \Delta A_2\ T_L + \Delta A_3\omega_r) = A_1 T_e + A_3\omega_r + d \tag{22}$$

and

$$d = (A_2 T_L + \Delta A_1 T_e + \Delta A_2\ T_L + \Delta A_3\omega_{rm}) \tag{23}$$

where $\Delta A_1, \Delta A_2, \Delta A_3$ are the variations of the parameters, and d is the uncertainty including the effects of the parameter variations and the external load.
Define the speed error e_2 as

$$e_2 = \omega_{rm}^* - \omega_{rm} \tag{24}$$

Taking the derivation of both sides, it is easy to obtain

$$\dot{e}_2 = \dot{\omega}_{\mathrm{rm}}^* - \dot{\omega}_{rm} \tag{25}$$

In this paper, we select a Lyapunov function as

$$\begin{aligned}\mathrm{V} &= \frac{1}{2}{e_2}^2 + \frac{1}{2}\frac{1}{\gamma}\tilde{d}^2 \\ &= \frac{1}{2}{e_2}^2 + \frac{1}{2}\frac{1}{\gamma}\left(d - \hat{d}\right)^2\end{aligned} \tag{26}$$

Taking the derivation of equation (26), it is easy to obtain

$$\begin{aligned}\dot{\mathrm{V}} &= e_2\dot{e}_2 + \frac{1}{\gamma}\tilde{d}\dot{\tilde{d}} \\ &= e_2\dot{e}_2 + \frac{1}{\gamma}\tilde{d}\left(\dot{d} - \dot{\hat{d}}\right) \\ &= e_2\dot{e}_2 - \frac{1}{\gamma}\tilde{d}\dot{\hat{d}}\end{aligned} \tag{27}$$

By substituting (25) into (27) and doing some arrangement, we can obtain

$$\begin{aligned}\dot{\mathrm{V}} &= e_2\left(\dot{\omega}_{rm}^{*} - \mathrm{A}_1 T_e - \mathrm{A}_3\omega_{rm} - d\right) - \frac{1}{\gamma}\tilde{d}\dot{\hat{d}} \\ &= e_2\left(\dot{\omega}_{rm}^{*} - \mathrm{A}_1 T_e - \mathrm{A}_3\omega_{rm} - \tilde{d} - \hat{d}\right) - \frac{1}{\gamma}\tilde{d}\dot{\hat{d}}\end{aligned} \tag{28}$$

Assume the torque can satisfy the following equation

$$T_e = \frac{1}{\mathrm{A}_1}\left(\dot{\omega}_{rm}^{*} - \mathrm{A}_3\omega_{rm} - \hat{d} + \mathrm{M}e_2\right) \tag{29}$$

Substituting (29) into (28), we can obtain

$$\dot{\mathrm{V}} = -\mathrm{M}{e_2}^2 - \tilde{d}e_2 - \frac{1}{\gamma}\tilde{d}\dot{\hat{d}} \tag{30}$$

From equation (30), it is possible to cancel the last two terms by selecting the following adaptive law

$$\dot{\hat{d}} = -\gamma e_2 \tag{31}$$

In equation (31), the convergence rate of the $\hat{d}$ is related to the parameter γ. By submitting (31) into (30), we can obtain

$$\dot{\mathrm{V}} = -\mathrm{M}{e_2}^2 \le 0 \tag{32}$$

From equation (32), we can conclude that the system is stable; however, we are required to use Barbalet Lemma to show the system is asymptotical stable [32]-[34].
By integrating equation (32), we can obtain

$$\int_0^{\infty} \dot{\mathrm{V}} d\tau = \mathrm{V}(\infty) - \mathrm{V}(0) < \infty \tag{33}$$

From equation (33), the integrating of parameter ${e_2}^2$ of the equation (32) is less than infinite. Then, $e_2(t) \in \mathrm{L}_\infty \cap \mathrm{L}_2$, and $\dot{e}_2(t)$ is bounded. According to Barbalet Lemma, we can conclude [32]-[34]

$$\lim_{t\to\infty} e_2(t) = 0 \tag{34}$$

The block diagram of the proposed adaptive backstepping control system is shown in Fig. 2, which is obtained from equations (29) and (31).

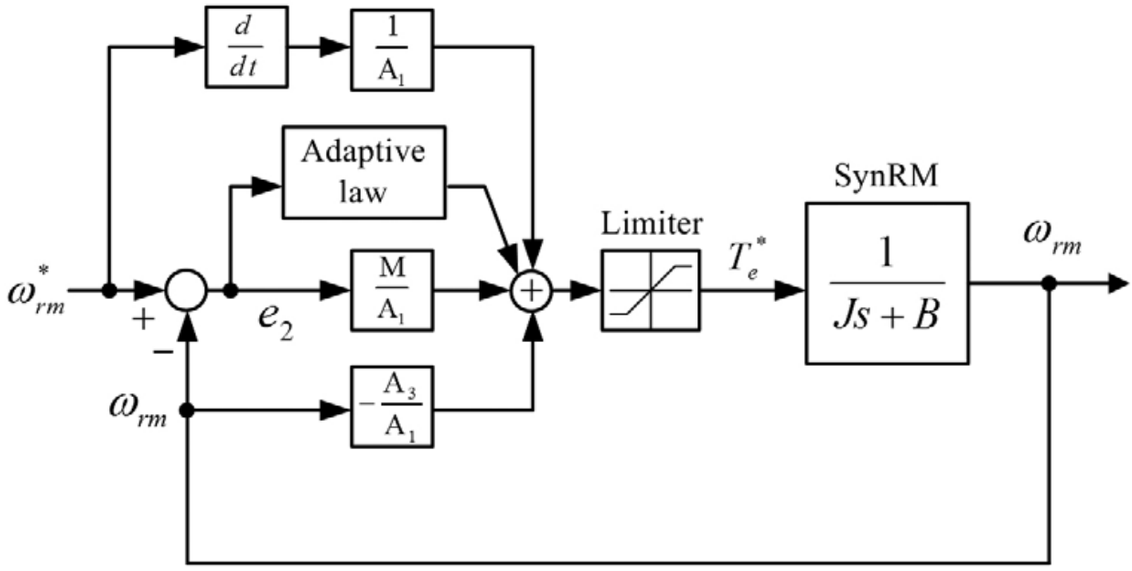

Fig. 2. The adaptive backstepping controller.

B. Model-Reference Adaptive Controller

Generally speaking, after the torque is applied, the speed of the motor incurs a delay of several micro seconds. As a result, the transfer function between the speed and the torque of a motor can be expressed as:

$$\frac{\omega_{rm}}{T_e} = \frac{1/J_m}{\left(s + B_m/J_m\right)} e^{-\tau s} \tag{35}$$

Where τ is the delay time of the speed response. In addition, the last term of equation (35) can be described as

$$e^{-\tau s} \cong \frac{1}{1+\tau s} \cong \frac{1/\tau}{s+1/\tau} \tag{36}$$

Substituting (36) into (35), one can obtain

$$\frac{\omega_{rm}}{T_e} = \frac{1/J_m}{(s + B_m/J_m)} \frac{1/\tau}{(s+1/\tau)} = \frac{b_0}{s^2 + a_1 s + a_0} \tag{37}$$

where

$$a_1 = \left(\frac{B_m}{J_m} + \frac{1}{\tau}\right) \tag{38a}$$

$$a_0 = \frac{B_m}{J_m \tau} \tag{38b}$$

$$b_0 = \frac{1}{J_m \tau} \tag{38c}$$

Equation (37) can be described as a state-space representation:

$$\begin{bmatrix} \dot{x}_1 \\ \dot{x}_2 \end{bmatrix} = \begin{bmatrix} 0 & 1 \\ -a_0 & -a_1 \end{bmatrix} \begin{bmatrix} x_1 \\ x_2 \end{bmatrix} + \begin{bmatrix} 0 \\ b_0 \end{bmatrix} u \tag{39a}$$

$$y = \begin{bmatrix} 1 & 0 \end{bmatrix} \begin{bmatrix} x_1 \\ x_2 \end{bmatrix} \tag{39b}$$

Where $x_1 = \omega_{rm} = y_p$, $x_2 = \dot{\omega}_{rm}$, and $u = T_e$. Next, the equations (39a) and (39b) can be rewritten as :

$$\dot{X}_p = A_p X_p + B_p u \tag{40a}$$

and

$$y_p = C_p^T X_p \tag{40b}$$

where

$$X_p = \begin{bmatrix} x_1 \\ x_2 \end{bmatrix} \tag{41a}$$

$$A_p = \begin{bmatrix} 0 & 1 \\ -a_0 & -a_1 \end{bmatrix} \tag{41b}$$

$$B_p = \begin{bmatrix} 0 \\ b_0 \end{bmatrix} \tag{41c}$$

$$C_p^T = \begin{bmatrix} 1 & 0 \end{bmatrix} \tag{41d}$$

After that, we define two state variables w_1 and w_2 as:

$$\dot{w}_1 = -h w_1 + u \tag{42}$$

and

$$\dot{w}_2 = -h w_2 + y_p \tag{43}$$

The control input u can be described as

$$u = Kr + Q_1 w_1 + Q_2 w_2 + Q_0 y_p \tag{44}$$

$$= \theta^T \phi$$

where

$$\theta^T = \begin{bmatrix} K & Q_1 & Q_2 & Q_0 \end{bmatrix}$$

and

$$\phi = \begin{bmatrix} r & w_1 & w_2 & y_p \end{bmatrix}^T$$

where γ is the reference command. Combining (40a),(42), and (43), we can obtain a new dynamic equation as

$$\begin{bmatrix} \dot{X}_p \\ \dot{w}_1 \\ \dot{w}_2 \end{bmatrix} = \begin{bmatrix} A_p & 0 & 0 \\ 0 & -h & 0 \\ C_p^T & 0 & -h \end{bmatrix} \begin{bmatrix} X_p \\ w_1 \\ w_2 \end{bmatrix} + \begin{bmatrix} B_p \\ 1 \\ 0 \end{bmatrix} u \tag{45}$$

Substituting (44) into (45), we can obtain

$$\begin{bmatrix} \dot{X}_p \\ \dot{w}_1 \\ \dot{w}_2 \end{bmatrix} = \begin{bmatrix} A_p + B_p Q_0 C_p^T & B_p Q_1 & B_p Q_2 \\ Q_0 C_p^T & -h + Q_1 & Q_2 \\ C_p^T & 0 & -h \end{bmatrix} \begin{bmatrix} X_p \\ w_1 \\ w_2 \end{bmatrix} + \begin{bmatrix} B_p K \\ K \\ 0 \end{bmatrix} r \tag{46}$$

Define $\tilde{K} = K - K^*$, $\tilde{Q}_1 = Q_1 - Q_1^*$, $\tilde{Q}_2 = Q_2 - Q_2^*$, $\tilde{Q}_0 = Q_0 - Q_0^*$
Then, equation (46) can be rearranged as

$$\begin{bmatrix} \dot{X}_p \\ \dot{w}_1 \\ \dot{w}_2 \end{bmatrix} = \begin{bmatrix} A_p + B_p Q_0^* C_p^T & B_p Q_1^* & B_p Q_2^* \\ Q_0^* C_p^T & -h + Q_1^* & Q_2^* \\ C_p^T & 0 & -h \end{bmatrix} + \begin{bmatrix} B_p K^* \\ K^* \\ 0 \end{bmatrix} r + \begin{bmatrix} B_p \\ 1 \\ 0 \end{bmatrix} \tilde{\theta}^T \phi \tag{47}$$

Where $\tilde{\theta}^T = \begin{bmatrix} \tilde{K} & \tilde{Q}_1 & \tilde{Q}_2 & \tilde{Q}_0 \end{bmatrix}$ is the parameter errors. It is possible to rearrange equation (47) as a simplified form

$$\dot{X}_c = A_m X_c + \begin{bmatrix} B_p K^* \\ K^* \\ 0 \end{bmatrix} r + B_m \tilde{\theta}^T \phi \tag{48}$$

and

$$Y_c = C_m^T X_c \tag{49}$$

where

$$X_c = \begin{bmatrix} X_p \\ w_1 \\ w_2 \end{bmatrix},\ A_m = \begin{bmatrix} A_p + B_p Q_0^* C_p^T & B_p Q_1^* & B_p Q_2^* \\ Q_0^* C_p^T & -h + Q_1^* & Q_2^* \\ C_p^T & 0 & -h \end{bmatrix},$$

$$B_m^T = \begin{bmatrix} B_p & 1 & 0 \end{bmatrix},\ C_m^T = \begin{bmatrix} C_p^T & 0 & 0 \end{bmatrix}.$$

After that, the referencing model of the closed-loop system can be described as :

$$\dot{X}_m = A_m X_m + B_m K^* r \tag{50}$$

and

$$Y_m = C_m^T X_m \tag{51}$$

where $X_m^T = \begin{bmatrix} X_p^* & w_1^* & w_2^* \end{bmatrix}$ is the vector of the state variables, and Y_m is the output of the referencing model. Now, we define the derivation of the state variable error and the output error as:

$$\dot{e} = \dot{X}_c - \dot{X}_m \tag{52}$$

and

$$e_1 = Y_c - Y_m \tag{53}$$

Substituting (50)-(51) into (52) and (53), one can obtain

$$\dot{e} = A_m e + B_m \tilde{\theta}^T \phi \tag{54a}$$

and

$$e_1 = C_m^T e \tag{54b}$$

By letting $\bar{B}_m = B_m K^*$, it is not difficult to rearrange (54a) as

$$\dot{e} = A_m e + \bar{B}_m \frac{1}{K^*} \tilde{\theta}^T \phi \tag{55a}$$

Combining (54b) and (55a), one can obtain

$$\dot{e}_1 = \frac{1}{K^*} C_m^T (sI - A_m)^{-1} \bar{B}_m \tilde{\theta}^T \phi \tag{56}$$

It is essential that the degree of the referencing model equal the uncontrolled plant. As a result, equation (55a) has to be revised as [12]:

$$\dot{e} = A_m e + \bar{B}_{m1} \frac{1}{K^*} \tilde{\theta}^T \bar{\phi} \tag{57a}$$

where $\bar{B}_{m1} = \bar{B}_m L_{(s)}$, $\bar{\phi} = L_{(s)}^{-1} \phi$, $L_{(s)} = s + F$; $F > 0$ ’

After that, we can obtain

$$\dot{e}_1 = \frac{1}{K^*} C_m^T \left(sI - A_m \right)^{-1} \bar{B}_{m1} \tilde{\theta}^T \bar{\phi} \tag{58}$$

Now, selecting a Lyapunov function as

$$\mathrm{V} = \frac{1}{2} e^T P_m e + \frac{1}{2} \tilde{\theta}^T \Gamma^{-1} \tilde{\theta} \left| \frac{1}{K^*} \right| \tag{59}$$

where P_m is a symmetry positive real matrix, and Γ is a positive real vector.
The matrix P_m satisfies the following two equations:

$$A_m^T P_m + P_m A_m = -\mathrm{Q} \tag{60}$$

and

$$P_m \bar{B}_{m1} = C_m^T \tag{61}$$

where Q is a symmetry positive real matrix . Taking the derivation of equation (59) and substituting (60), (61) into the derivation equation, we can obtain

$$\begin{aligned} \dot{\mathrm{V}} &= \frac{-1}{2} e^T \mathrm{Q} e + e^T P_m \bar{B}_{m1} \frac{1}{K^*} \tilde{\theta}^T \bar{\phi} + \tilde{\theta}^T \Gamma^{-1} \dot{\tilde{\theta}} \left| \frac{1}{K^*} \right| \\ &= \frac{-1}{2} e^T \mathrm{Q} e + e_1 \frac{1}{K^*} \tilde{\theta}^T \bar{\phi} + \tilde{\theta}^T \Gamma^{-1} \dot{\tilde{\theta}} \left| \frac{1}{K^*} \right| \end{aligned} \tag{62}$$

It is possible to select the adaptive law as

$$\dot{\theta} = -\mathrm{sgn}\left(\frac{1}{K^*} \right) \Gamma e_1 \bar{\phi} \tag{63}$$

where $\mathrm{sgn}\left(\frac{1}{K^*} \right) = \frac{\left| K^* \right|}{K^*}$, substituting (63) into (62), we can obtain :

$$\dot{\mathrm{V}} = \frac{-1}{2} e^T \mathrm{Q} e \le 0 \tag{64}$$

Next, by using Barbalet Lemma, we can obtain that the system is asymmetrical and

$$\lim_{t \to \infty} e_1(t) = 0 \tag{65}$$

Finally, we can obtain

$$
\begin{aligned}
u_p &= L_{(s)}\theta^T L_{(s)}{}^{-1}\phi = L_{(s)}\theta^T\bar{\phi} \\
&= \dot{\theta}^T\bar{\phi} + \theta^T\dot{\bar{\phi}} + F\theta^T\bar{\phi} = \dot{\theta}^T\bar{\phi} + \theta^T\phi
\end{aligned}
\tag{66}
$$

The block diagram of the model-reference control system is shown in Fig. 3, which includes referencing model, adaptive controller, and adaptive law.

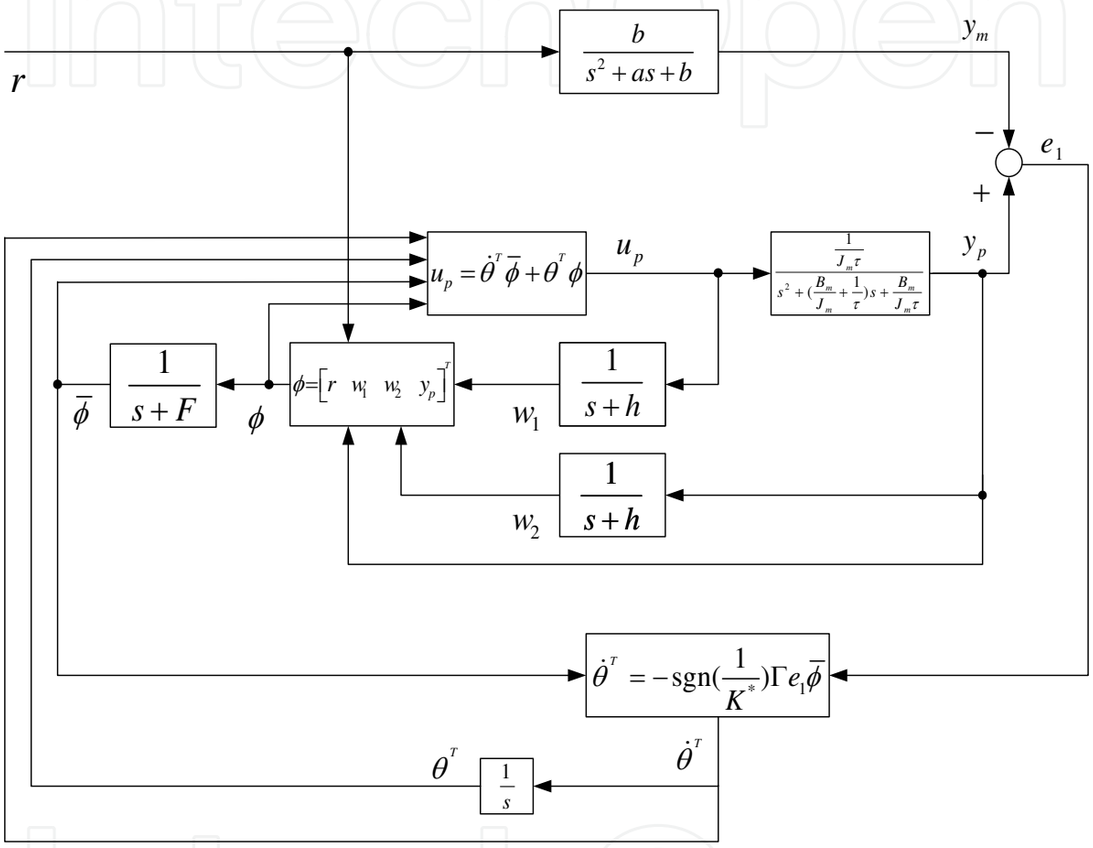

Fig. 3. The block diagram of the model reference adaptive controller.

4. Implementation

The implemented system is shown in Fig. 4. The system includes two major parts: the hardware circuits and the software programs. The hardware circuits include: the synchronous reluctance motor, the driver and inverter, the current and voltage sensors, and the A/ D converters. The software programs consist of the torque estimator, the flux estimator, the speed estimator, the adaptive speed controller, and the direct torque control algorithm. As you can observe, the most important jobs are executed by the digital signal processor; as a result, the hardware is quite simple. The rotor position can be obtained by stator flux, which is computed from the stator voltages and the stator currents. The digital signal processor outputs triggering signals every 50 μs ; as a result, the switching frequency of the inverter is 20 kHz. In addition, the sampling interval of the speed control loop is 1 ms

although the adaptive controllers are quite complicated. The whole drive system, therefore, is a multi-rate fully digital control system.

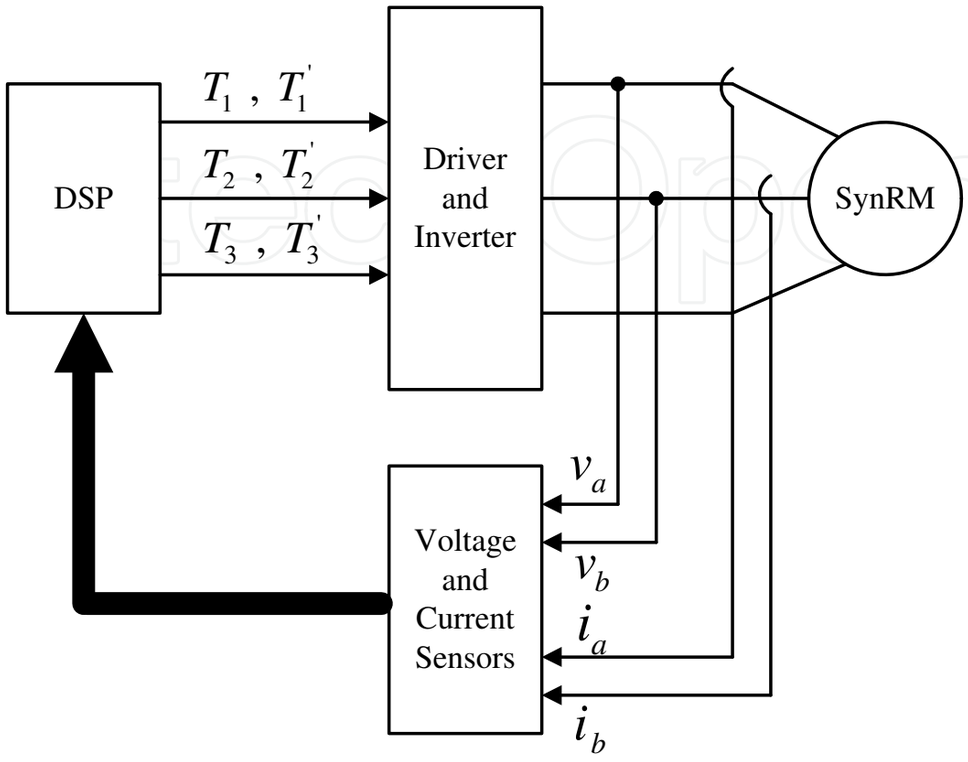

Fig. 4. The implemented system.

A. Hardware Circuits

The hardware circuits of the synchronous reluctance drive system includes the major parts. The details are discussed as follows.

a. The delay circuit of the IGBT triggering signals.

Fig. 5 shows the proposed delay circuit of the IGBT triggering signals. The delay circuit is designed to avoid the overlapping period of the turn-on interval of the upper IGBT and the lower IGBT for the inverter. Then, the inverter can avoid a short circuit. In this paper, the delay time of the delay circuit is set as 2 μs . To achieve the goal, two integrated circuit chips are used: 74LS174 and 74LS193. The basic idea is described as follows. First, the digital signal processor sends a clock signal to 74LS193. The time period of the clock is 62.5 μs . The 74LS193 executes the dividing frequency function and finally generates a clock signal with a 0.5 μs period. After that, the 74LS193 sends it into the CLK pin of 74LS174. The 74LS174 provides 6 series D-type flip-flop to generate a 3 μs delay. Finally, an AND gate is used to make a 3 μs for a rising-edge triggering signal but not a falling-edge triggering signal.

b. The driver of the IGBTs

The power switch modules used in the paper are IGBT modules, type 2MBI50-120. Each module includes two IGBTs and two power diodes. The driver of the IGBT is type EX-B840, made by Fuji company. The detailed circuit of the driver for an IGBT is shown in Fig. 6. In Fig. 6, the EX-B840, which is a driver, uses photo-couple to convert the control signal into a

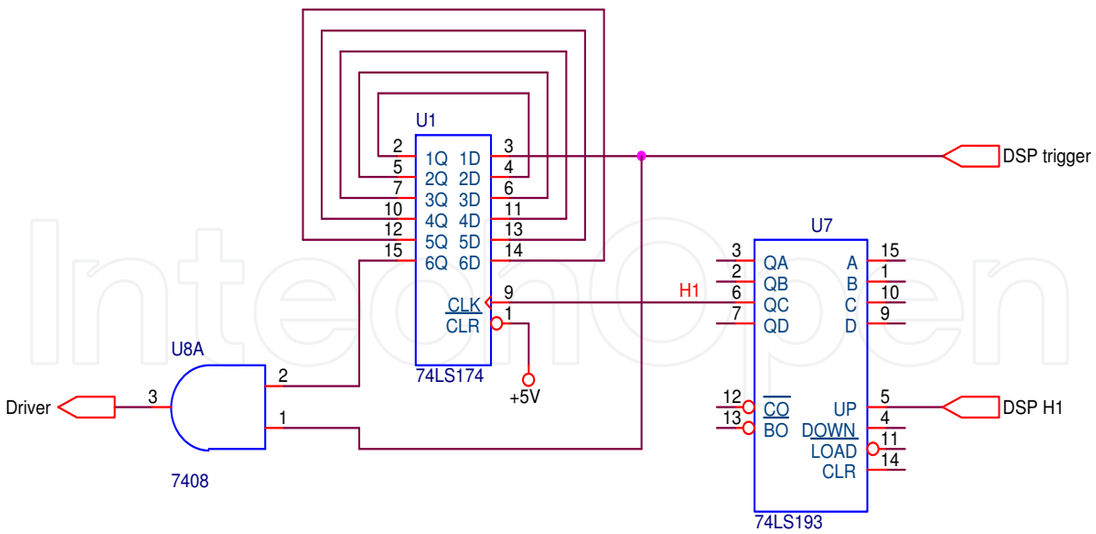

Fig. 5. The delay circuit of the IGBT triggering signals.

triggering signal for an IGBT. In addition, the EX-B840 provides the isolation and over-current protection as well.

When the control signal is "High", the photo transistor is turned on. Then, the photo diode is conducted. A 15V can across the gate and emitter of the IGBT to turn on the IGBT. On the other hand, when the control signal is "Low", the photo transistor is turned off. As a result, the photo diode is cut off. A -5V can across the gate and emitter of the IGBT to make IGBT turn off immediately.

The protection of the IGBT is included in Fig. 6. When the IGBT has over-current, the voltage across the collector and emitter of the IGBT is obviously dropped. After the 6-pin of EX-B840 detects the dropped voltage, the 5-pin of the EX-B840 sends a "Low" voltage to the photo diode. After that, the photo diode is opened, and a -5V across the gate and emitter of the IGBT is sent to turn off the IGBT.

c. The snubber circuit

The snubber circuit is used to absorb spike voltages when the IGBT is turned off. As we know, the synchronous reluctance motor is a kind of inductive load. In Fig. 7, when the upper leg IGBT T is turned off, the low leg IGBT T' cannot be turned on immediately due to the required dead-time, which can avoid short circuits. A new current path to keep the current continuous flow is required. The new current path includes the fast diode D and the snubber capacitor C_s. So, the current can flow through the fast diode D and the capacitor C_S, and then stores its energy into the capacitor C_S. On the other hand, when the IGBT is turned on in next time interval, the stored energy in the capacitor C_S can flow through the resistance R_s and the IGBT T. Finally, the energy dissipates in the resistance R_s. By suitably selecting the parameter C_s and R_s, a snubber circuit with satisfactory performance can be obtained.

d. The current detecting circuit

The current detecting circuit is used to measure the stator current of the synchronous reluctance motor, and can be shown in Fig. 8. The Hall current sensor, typed LP-100, is used to sense the stator current of the motor and to provide the isolation between the power stage

and the control circuit. The primary side of the LT-100P can measure 0 to 100 A with a bandwidth of 100 kHz. The basic principle is discussed as follows. The primary of the LT-100P has 5 turns. As a result, when 1A flows into the primary side, the secondary side of the LT-100P can generate 5mA. The current flows from the M pin of the LP-100P to the 0.1 $K\Omega$ resistance, and then provides 0.5V voltage drop. As a result, in this chapter, for every 1A primary current, the circuit can output 0.5V. A low-pass filter is designed to eliminate the high-frequency noise.

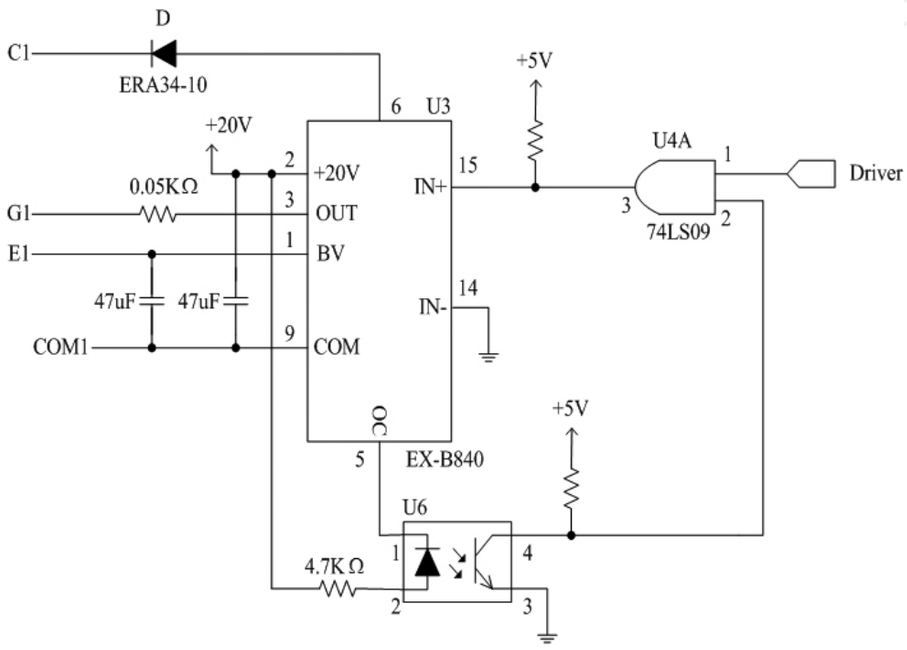

Fig. 6. The circuit of the driver for IGBTs.

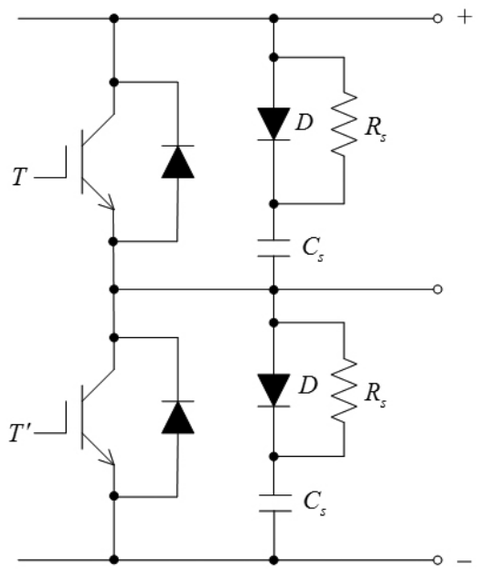

Fig. 7. The snubber circuit.

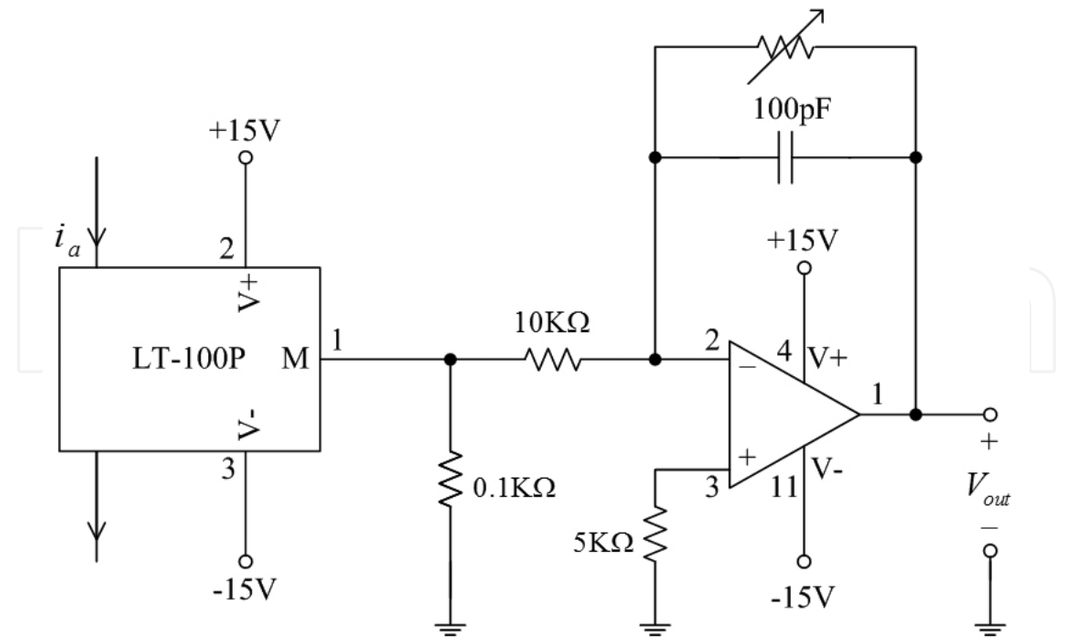

Fig. 8. The current detecting circuit.

e. The voltage detecting circuit

The voltage detecting circuit is used to sense the stator voltage of the synchronous reluctance motor, which is an important item for computing the estimated flux of the motor. A voltage isolation amplifier, AD210, is selected to isolate the input side and output side. In the chaper, R_0 and R_1 are used to attenuate the input voltage to be 0.05 v_{ab} . As a result, the input of AD 210 is limited under $\pm 10V$.

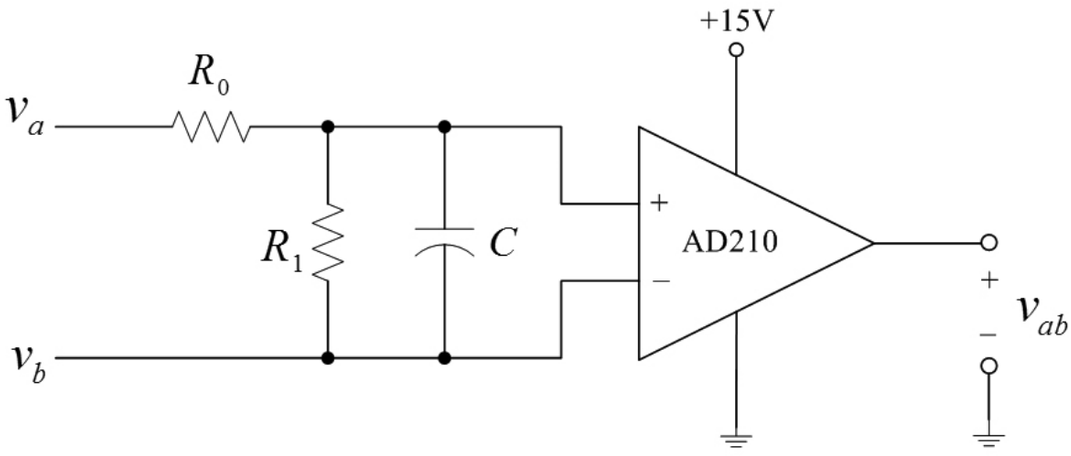

Fig. 9. The voltage detecting circuit.

f. The A/ D conversion circuit

The measured voltages and currents from Hall current sensor and AD210 are analog signals. In order to be read by a digital signal processor, the A/ D conversion is required. In this chapter, the 12 bit A/ D converter with a 3 μs conversion time is used. The A/ D converter is

typed AD578. The detailed circuit is shown in Fig. 10. There are two sets: one for voltage conversion, and the other for current conversion.

When the analog signal is ready, the digital signal processor outputs a triggering signal to the A/ D converter. Then, each AD578 converter starts to convert the analog signal into a digital signal. When the conversion process finishes, an EOC signal is sent from the AD578 to latch the 74LS373. Next, the digital signal processor reads the data. In this chapter, a timer with a fixed clock is used to start the conversion of the AD578 and then the digital signal processor can read the data. By using the method, we can simplify the software program of the digital signal processor.

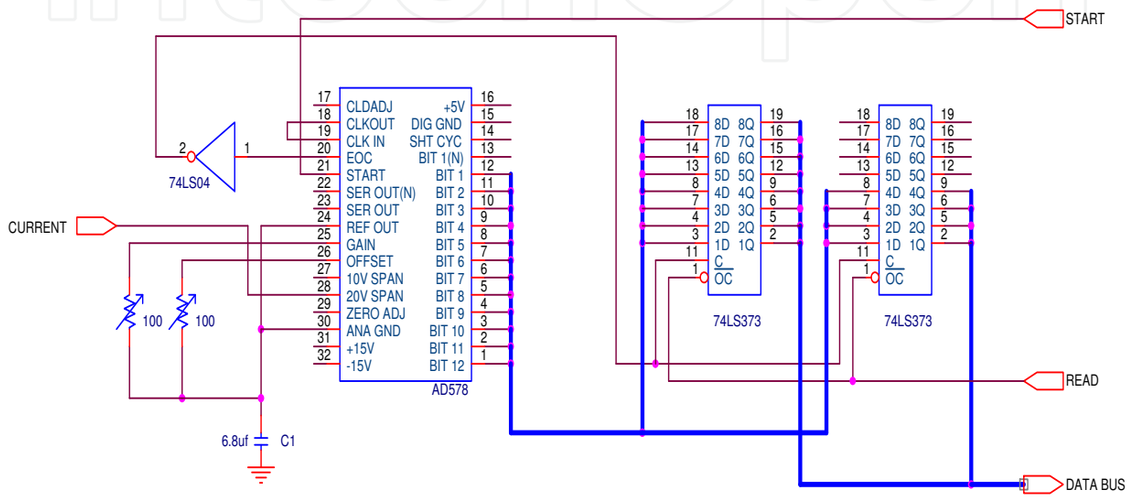

Fig. 10. A/ D converter circuit.

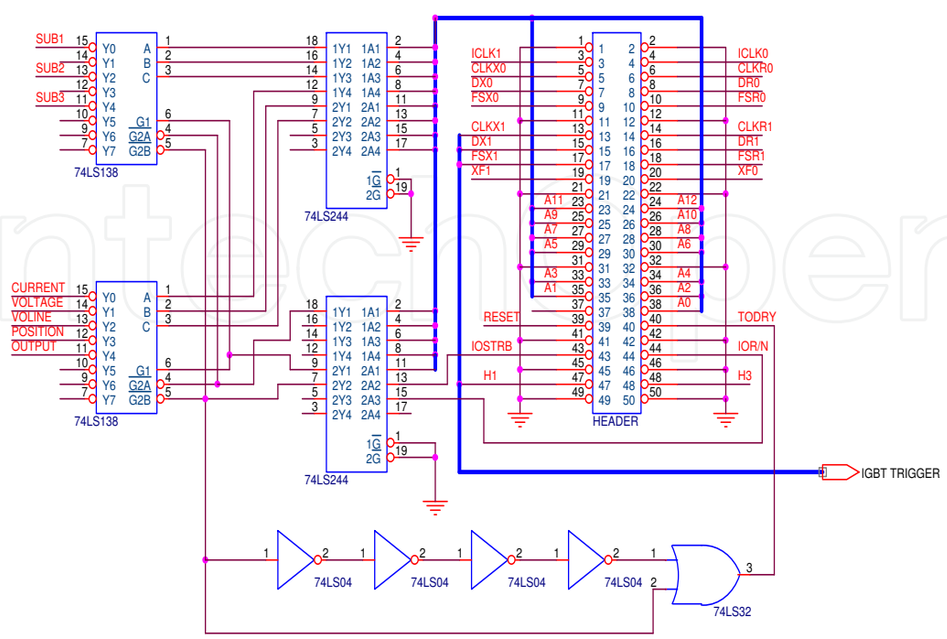

Fig. 11. The interfacing circuit of the DSP.

g. The interfacing circuit of the digital signal processor

In the chapter, the digital signal processor, type TMS320-C30, is manufactured by Texas Instruments. The digital signal processor is a floating-point operating processor. The application board, developed by Texas Instruments, is used as the major module. In addition, the expansion bus in the application board is used to interface to the hardware circuit. The voltage, current, speed, and rotor position of the drive system are obtained by using the expansion bus. As a result, the address decoding technique can be used to provide different address for data transfer. In addition, the triggering signals of the IGBTs are sent by the following pins: CLKX1, DX1, and FSX1. The details are shown in Fig. 11.

A. Software Development

a. The Main Program

Fig. 12 shows the flowchart of the initialization of the main program. First, the DSP enables the interrupt service routine. Then, the DSP initializes the peripheral devices. Next, the DSP sets up parameters of the controller, inverter, A/ D converter, and counter. After that, the DSP enables the counter, and clear the register. Finally, the DSP checks if the main program is ended. If it is ended, the main program stops; if it is not, the main program goes back to the initializing peripheral devices and carries out the following processes mentioned.

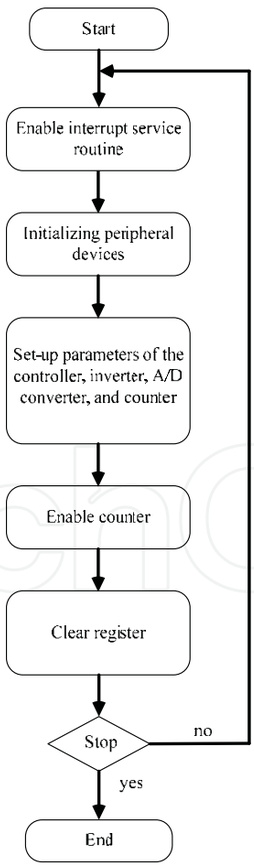

Fig. 12. The flowchart of the initialization of the main program.

b. The interrupt service routines

The interrupt service routines include: the backstepping adaptive controller, the reference model adaptive controller, and the switching method of the inverter. The detailed flowcharts are shown in Fig. 13, Fig. 14, and Fig. 15.

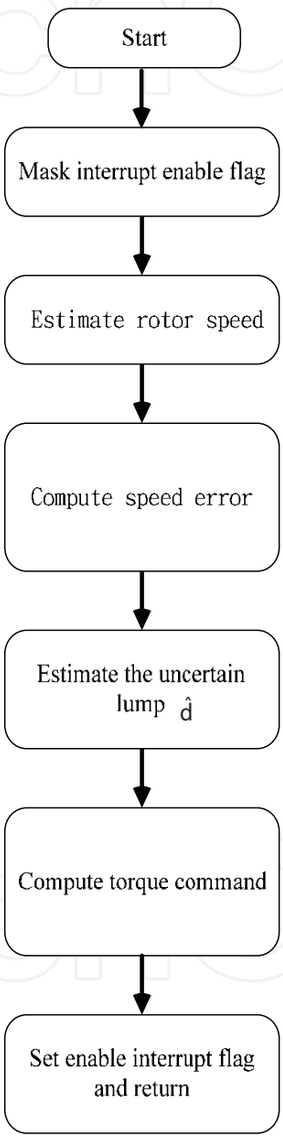

Fig. 13. The subroutine of the backstepping adaptive controller.

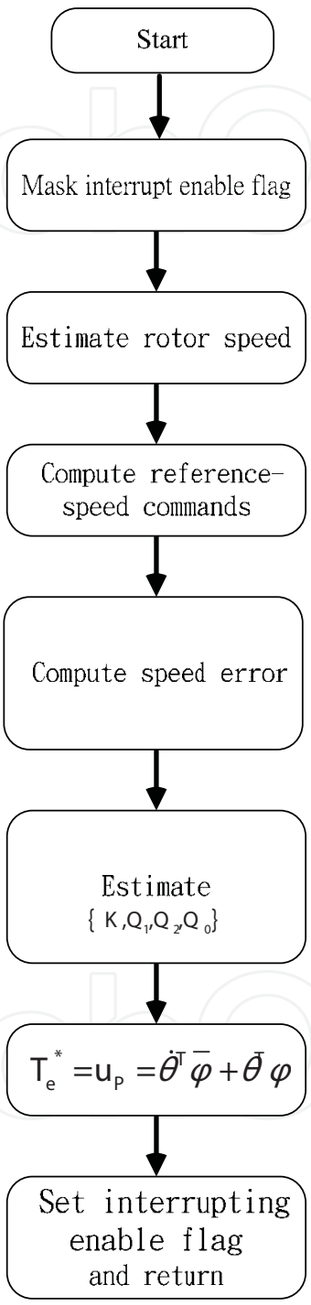

Fig. 14. The subroutine of the reference model adaptive controller.

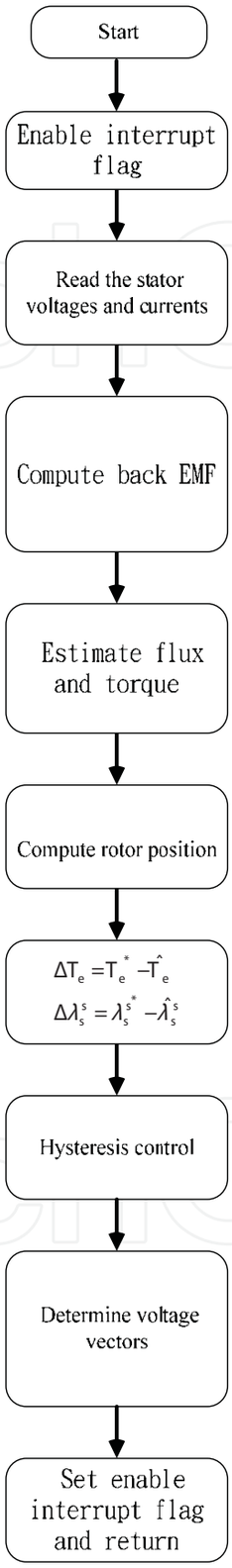

Fig. 15. The subroutine of the switching method of the inverter.

5. Experimental results

Several experimental results are shown here. The input dc voltage of the inverter is 150V. The switching frequency of the inverter is 20 kHz. In addition, the sampling interval of the minor loop is 50 μs, and the sampling interval of the speed loop is 1 ms. The parameters of the PI controller are K_P =0.006 and K_I =0.001. The parameters of the adaptive backstepping controller are M=3 and γ =0.8. The parameters of the model referencing controller are Γ = [-0.0002 -0.004 -0.004 -0.0006]. Fig. 16(a)(b) show the measured steady-state waveforms. Fig. 16(a) is the measured a-phase current and Fig. 16(b) is the measured line-line voltage, v_{ab}. Fig. 17(a) is the simulated fluxes at 1000 r/ min. Fig. 17(b) is the simulated flux trajectory at 1000 r/ min. Fig. 17(c) is the measured fluxes at 1000 r/ min. Fig. 17(d) is the measured flux trajectory at 1000 r/ min. As you can observe, the trajectories are both near circles in both simulation and measurement. Fig. 18(a) shows the comparison of the measured estimating rotor angle and the measured real rotor angle at 50 r/ min. As we know, when the motor is operated at a lower speed, the flux becomes smaller. As a result, the motor cannot be operated well at lower speeds due to its small back emf. The estimating error, shown in Fig. 18(b) is obvious. Fig. 19(a)(b) show the measured estimating rotor angle at 1000 r/ min. Fig. 19(a) shows the comparison of the measured estimating rotor angle and the measured real rotor angle at 1000 r/ min. Fig. 19(b) shows the estimating error, which is around 2 degrees. As a result, the estimating error is reduced when the motor speed is increased. In addition, Fig. 19(b) is varied more smoothly than the Fig. 18(b) is. The major reason is that the back emf has a better signal/ noise ratio when the motor speed increases. Fig. 20(a) shows the measured transient responses at 50 r/ min. Fig. 20(b) shows the measured load disturbance responses under 2 N.m external load. The model reference control performs the best. The steady-state errors of Fig. 20(a)(b) are: 2.7 r/ min for PI controller, 0.5 r/ min for ABSC controller, and 0.1 r/ min for MRAC controller, respectively. According to the measured results, the MRAC controller performs the best and the PI controller performs the worst in steady-state. Fig. 21(a)(b) show the measured speed responses at 1000 r/ min. Fig. 21(a) is the measured transient responses. Fig. 21(b) is the load disturbance responses under 2 N.m. According to the measured results, the model-reference controller performs better than the other two controllers in both transient response and load disturbance response again. The steady-state errors of Fig. 21(a)(b) are: 7.3 r/ min for PI controller, 1.9 r/ min for ABSC controller, and 0.1 r/ min for MRAC controller, respectively. As you can observe, the conclusions are similar to the results of Fig. 20(a)(b). Fig. 22(a) shows the measured external - $\hat{d}$ of the adaptive backstepping control. Fig. 22(b) shows the measured speed error of the adaptive backstepping control by selecting different parameters. Fig. 23(a)(b)(c)(d) show the relative measured parameters K, K, Q_1, Q_2, Q_0 of the model-reference controller. All the parameters converge to constant values. Fig. 24(a)(b)(c) show the measured speed responses of a triangular speed command. The PI controller has a larger steady-state error than the adaptive controllers have. Fig. 25(a)(b)(c) show the measured speed responses of a sinusoidal speed command. As you can observe, the model-reference controller performs the best. The model- reference controller has a smaller steady-state error and performs a better tracking ability than the other controllers.

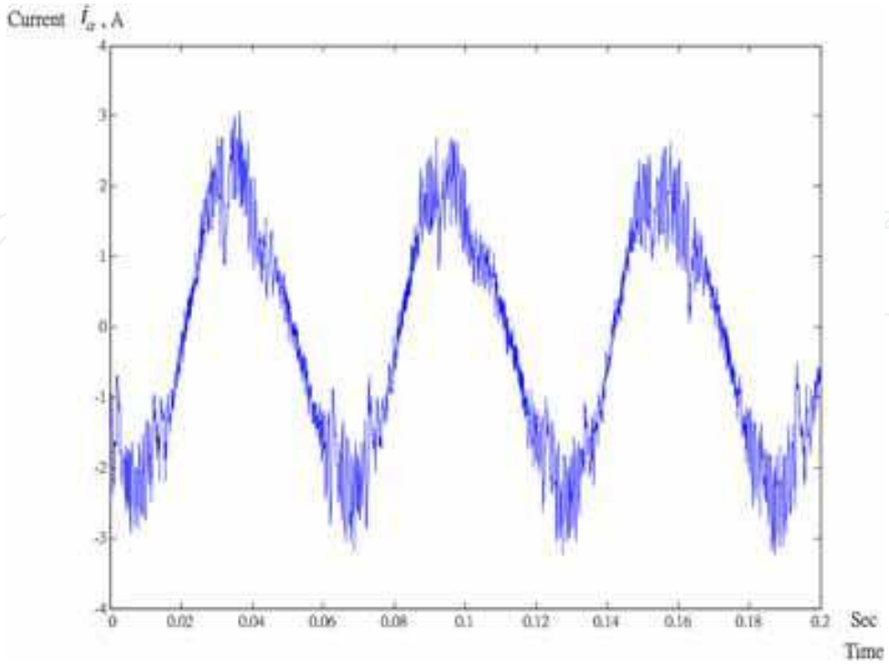

(a)

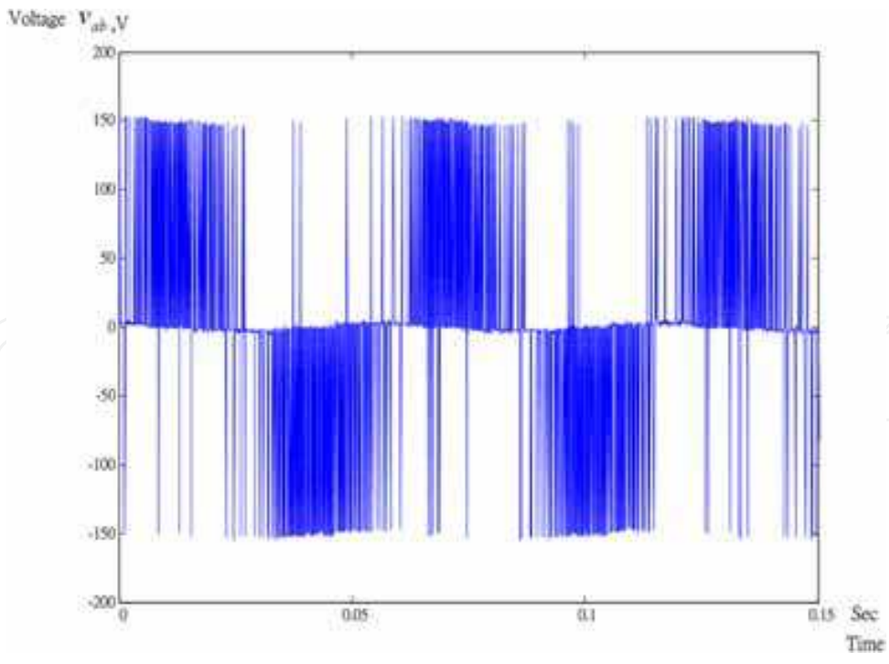

(b)

Fig. 16. The measured steady-state waveforms. (a) phase current (b) line voltage.

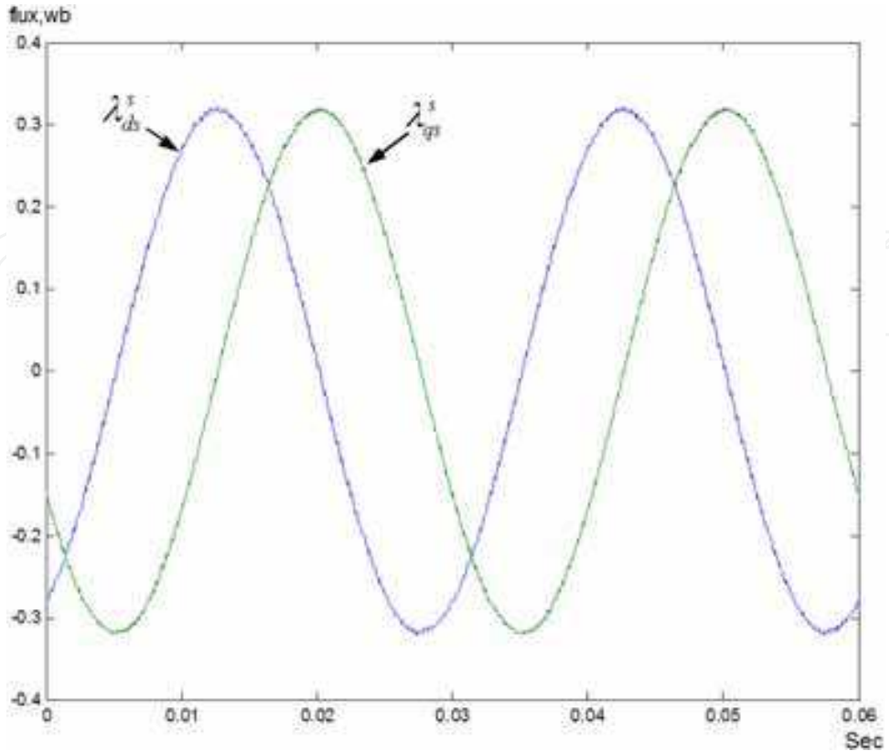
flux,wb
0.4
0.3
0.2
0.1
0
-0.1
-0.2
-0.3
-0.4
λ^s_{ds}
λ^s_{qs}
0
0.01
0.02
0.03
0.04
0.05
0.06
Sec

(a)

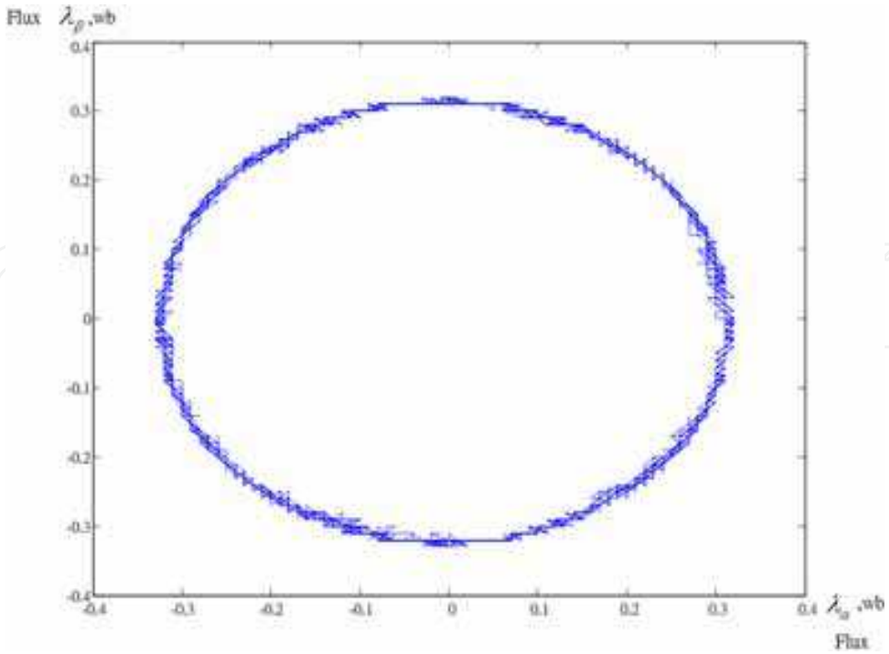
Flux λ_q,wb
0.4
0.3
0.2
0.1
0
-0.1
-0.2
-0.3
-0.4
-0.4
-0.3
-0.2
-0.1
0
0.1
0.2
0.3
0.4
λ_d ,wb
Flux

(b)

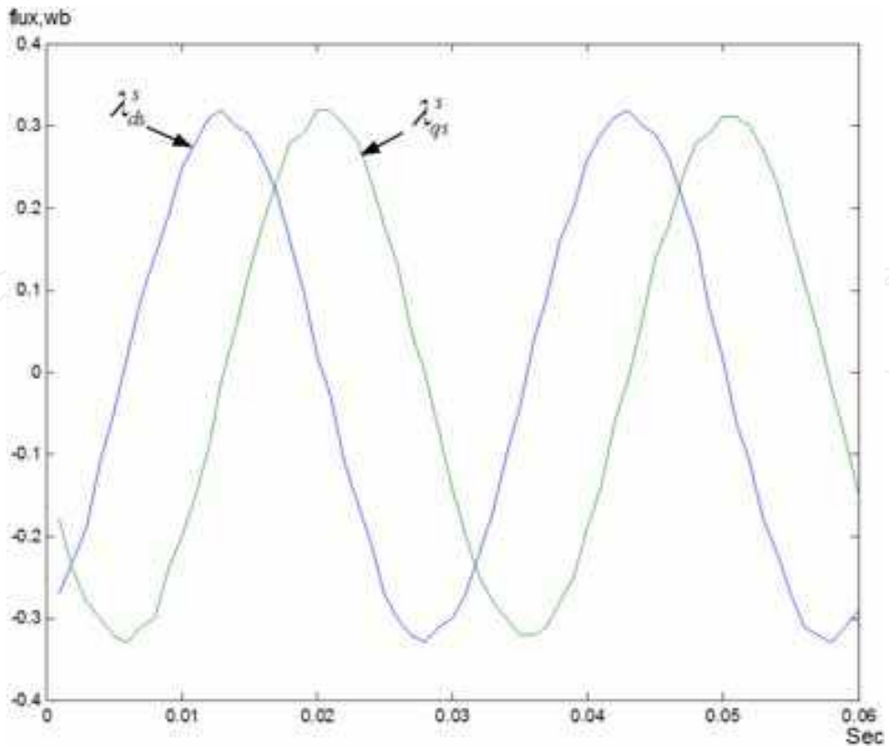

(c)

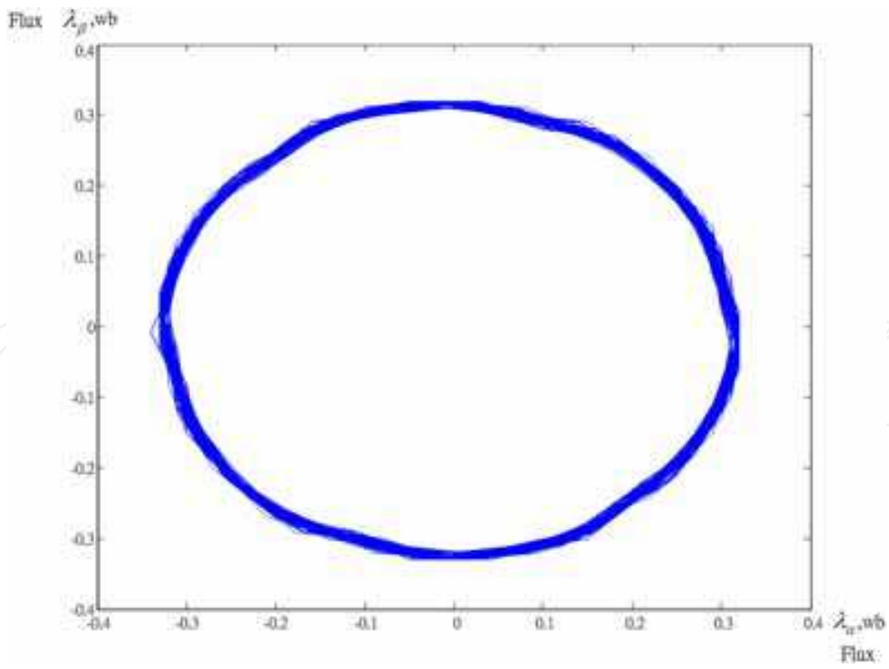

(d)

Fig. 17. The stator flux trajectories at 1000 r/ min. simulated fluxes (b) simulated trajectory (c) measured fluxes (d) measured trajectory.

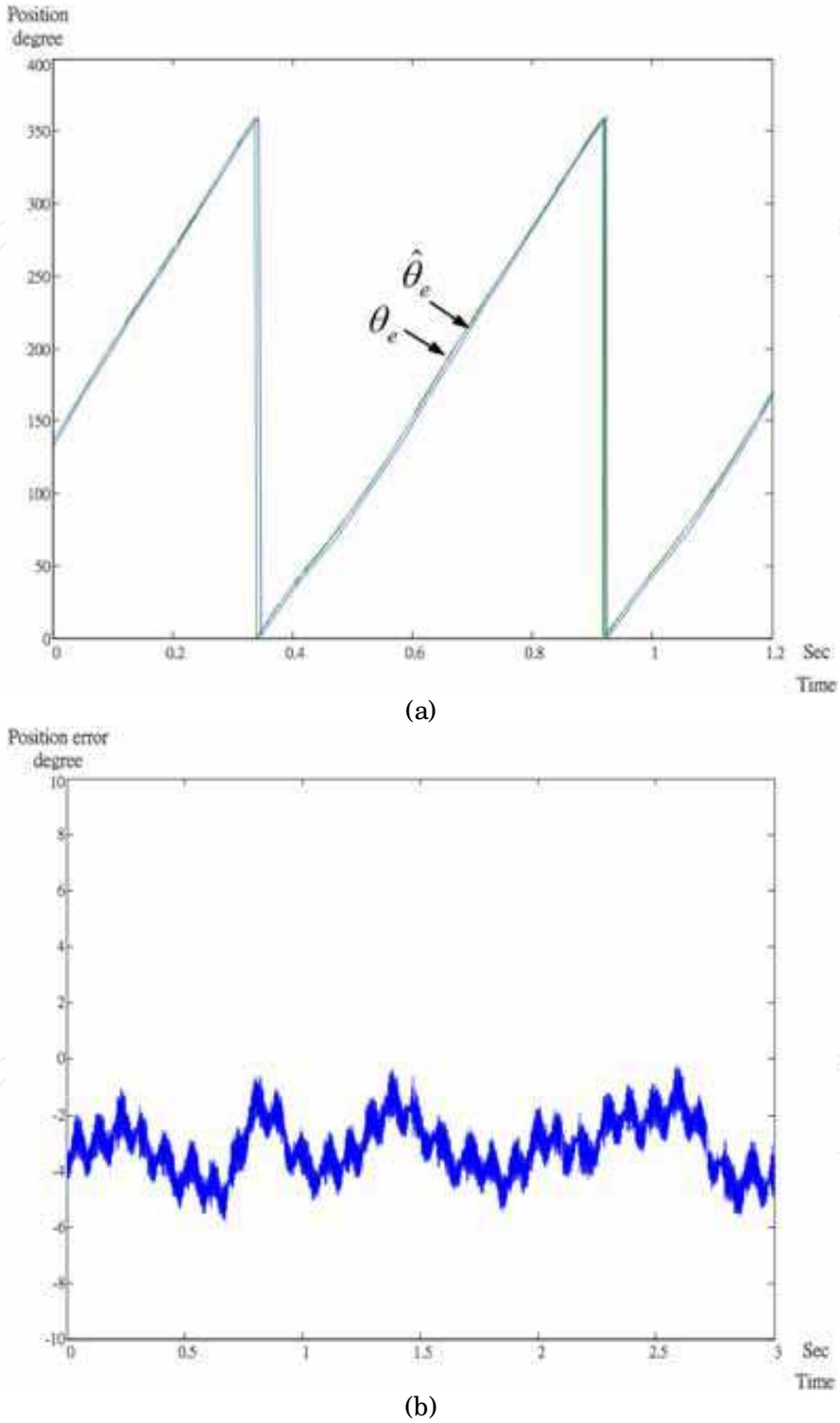

Fig. 18. The measured estimating rotor angle at 50 r/ min. (a) comparison (b) estimating error.

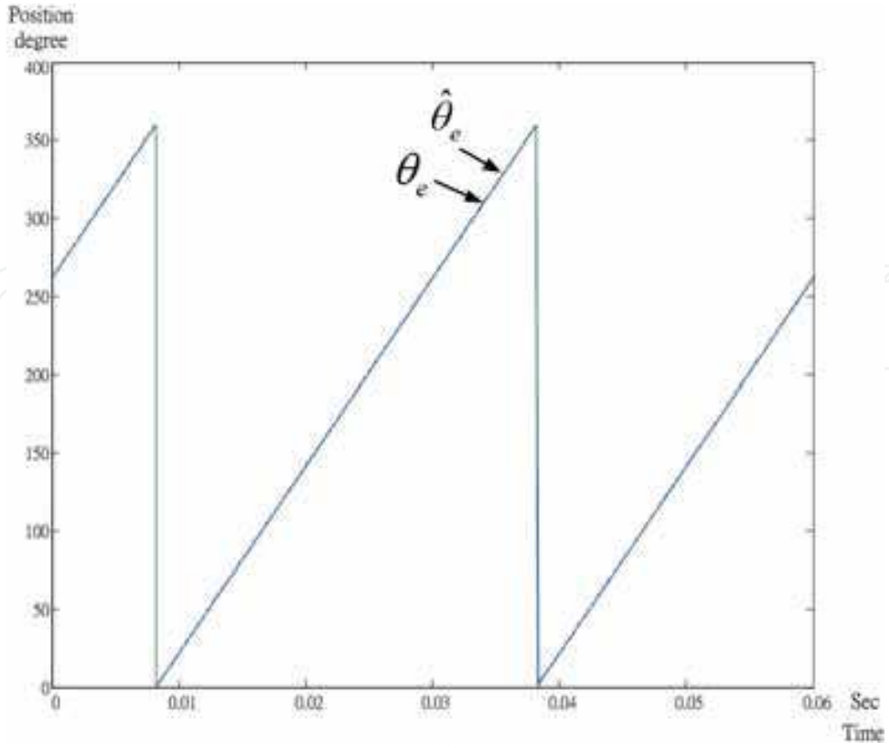

(a)

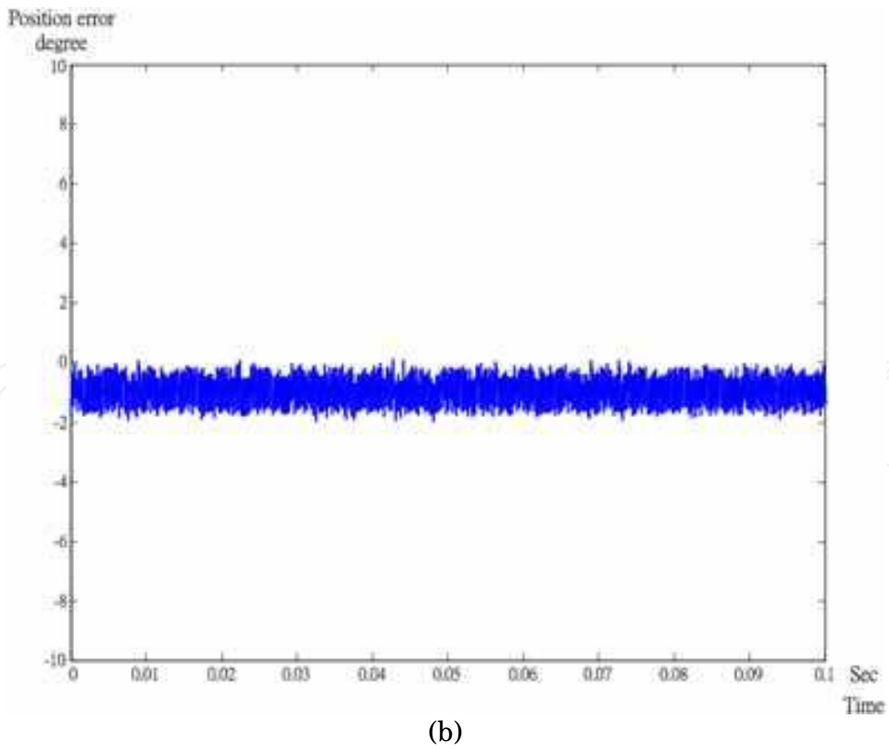

(b)

Fig. 19. The measured estimating rotor angle at 1000 r/ min. (a) comparison (b) estimating error.

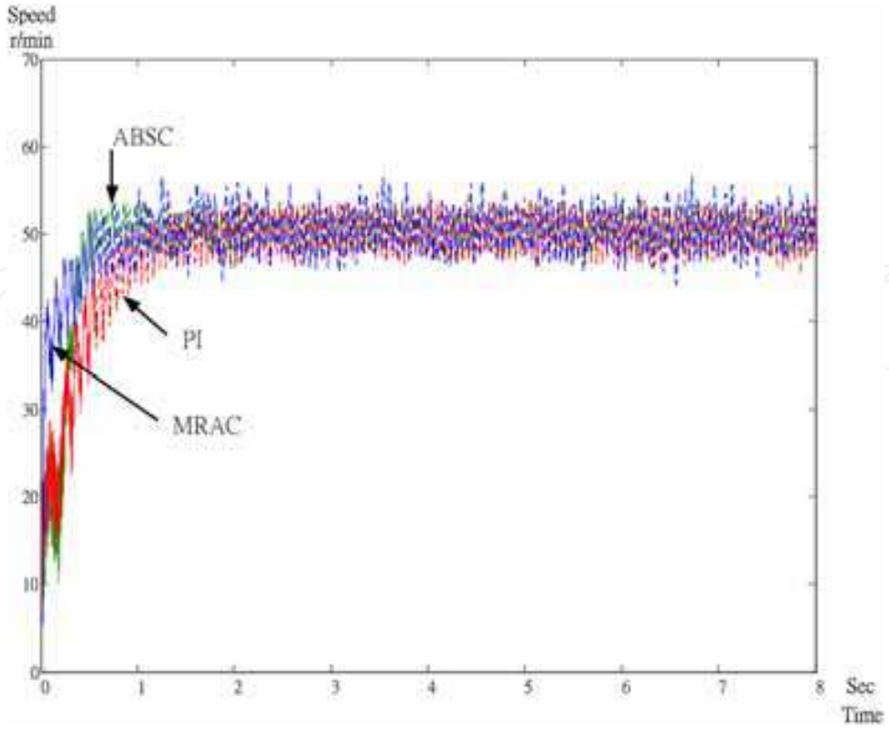

(a)

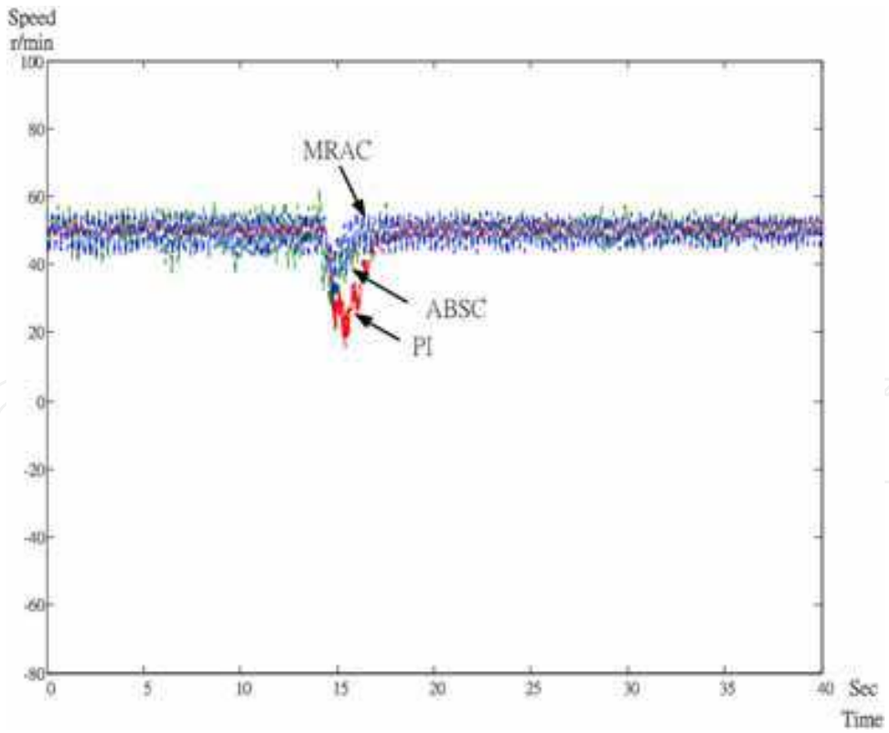

(b)

Fig. 20. The measured speed responses at 50 r/ min, (a) transient responses (b) load disturbance responses

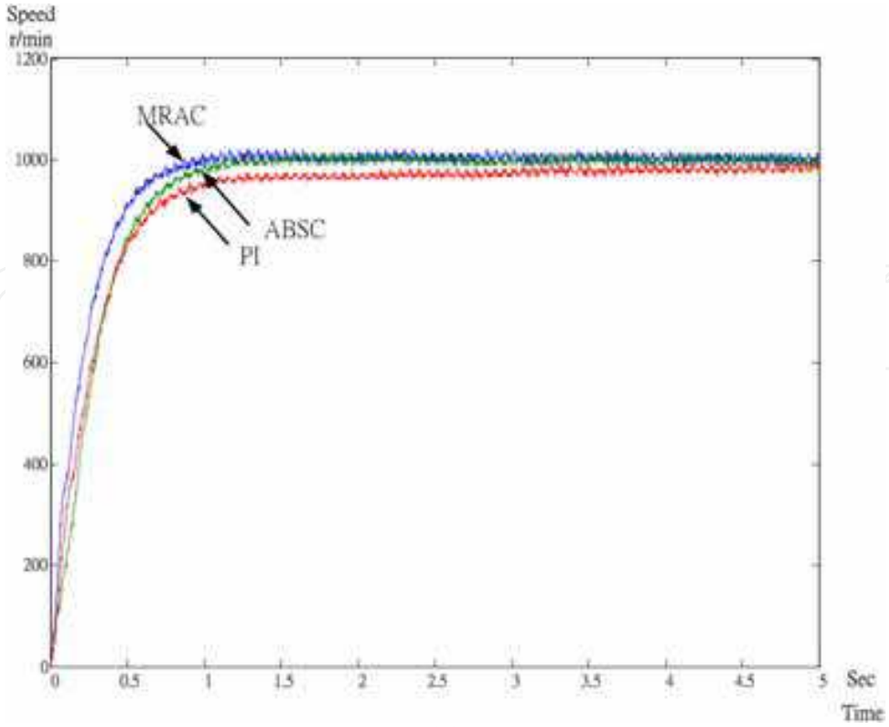

(a)

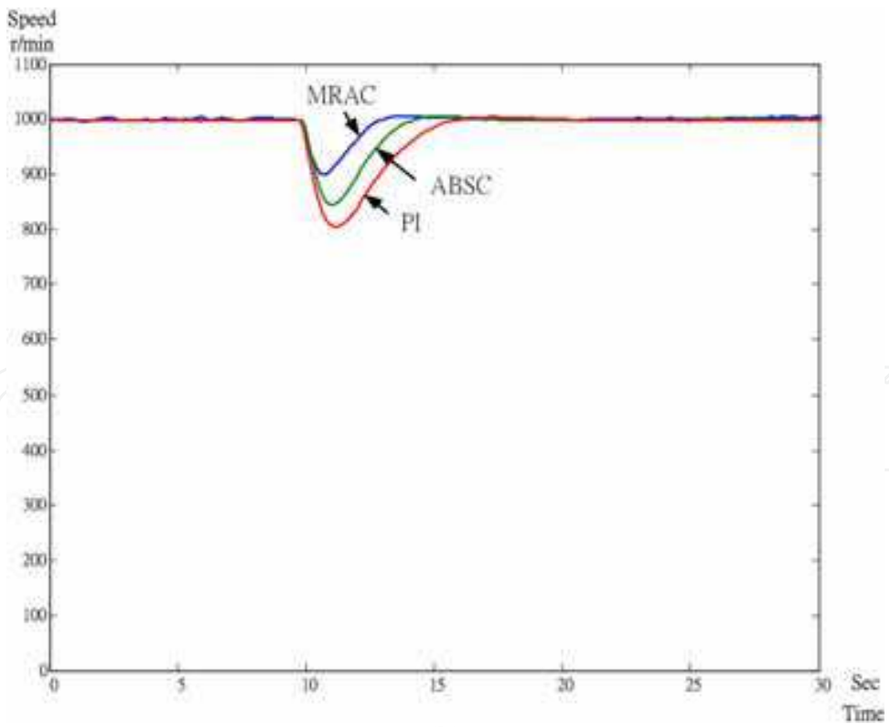

(b)

Fig. 21. The measured speed responses at 1000 r/ min. (a) transient responses (b) load disturbance responses.

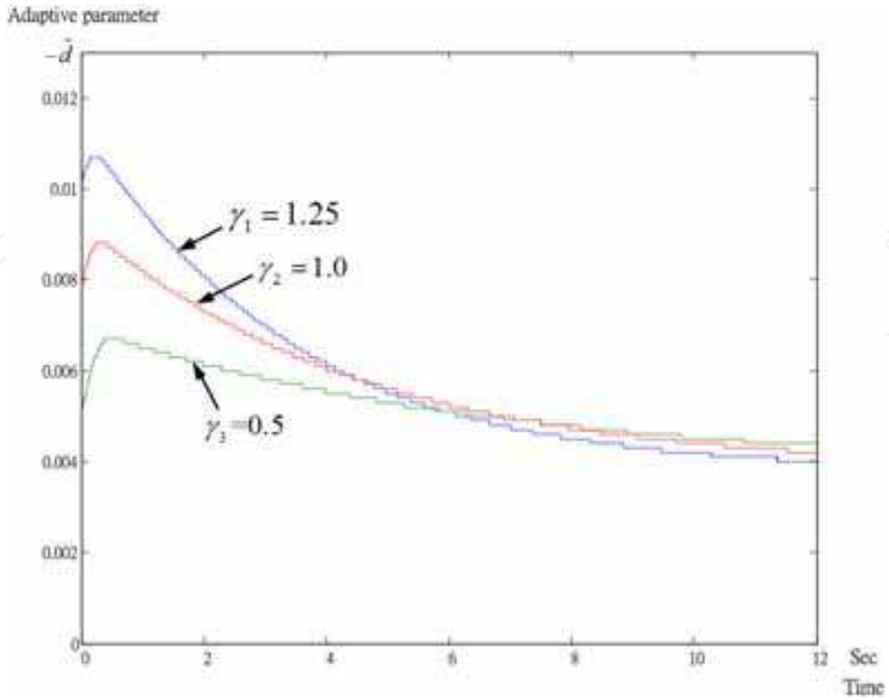

(a)

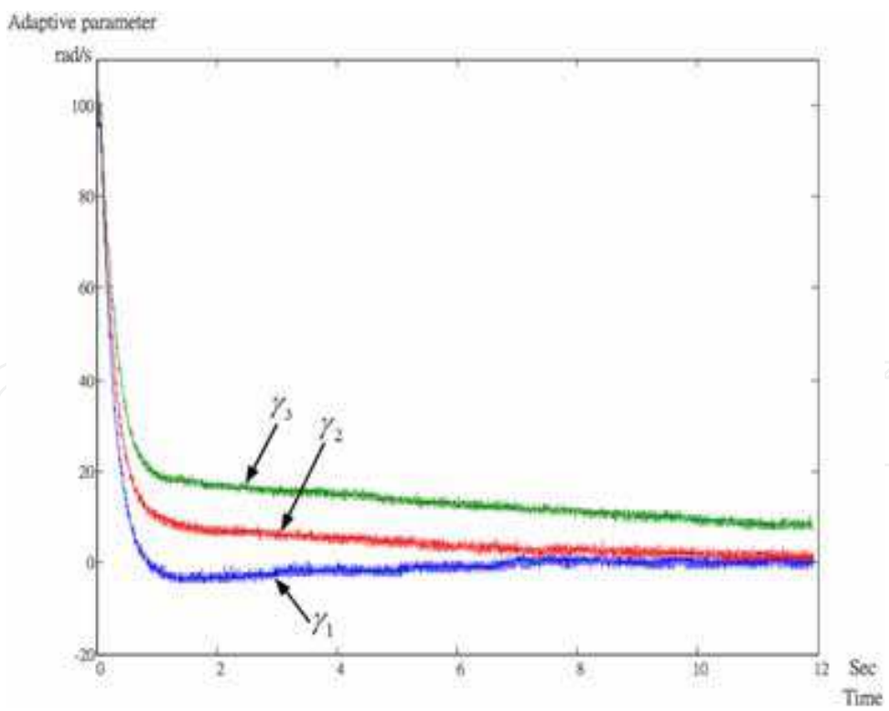

(b)

Fig. 22. The measured responses of adaptive backstepping control. (a) $-\hat{d}$ (b) speed error.

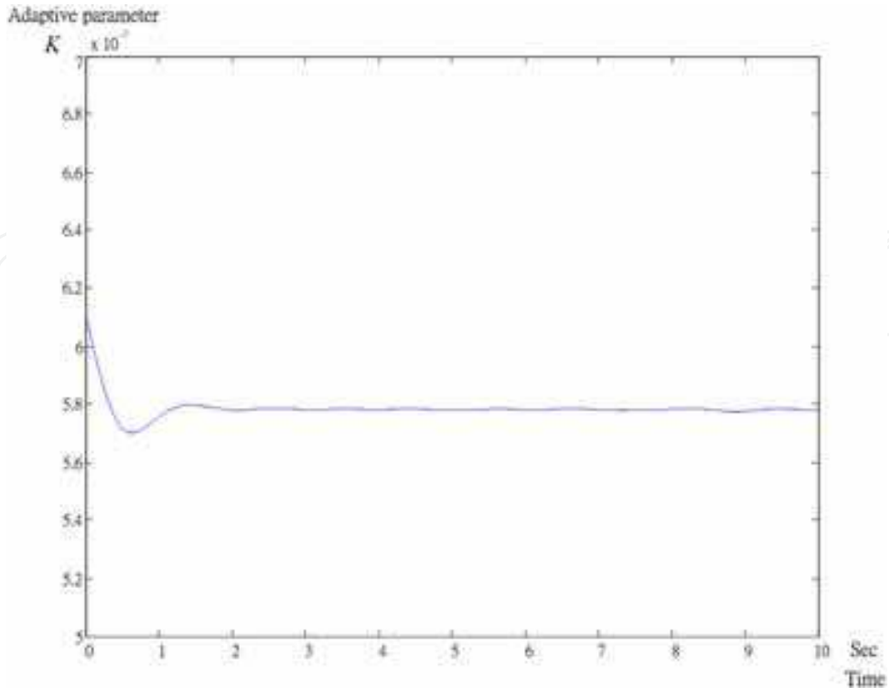
Adaptive parameter
K
x 10^-2
7
6.8
6.6
6.4
6.2
6
5.8
5.6
5.4
5.2
5
0 1 2 3 4 5 6 7 8 9 10
Sec
Time

(a)

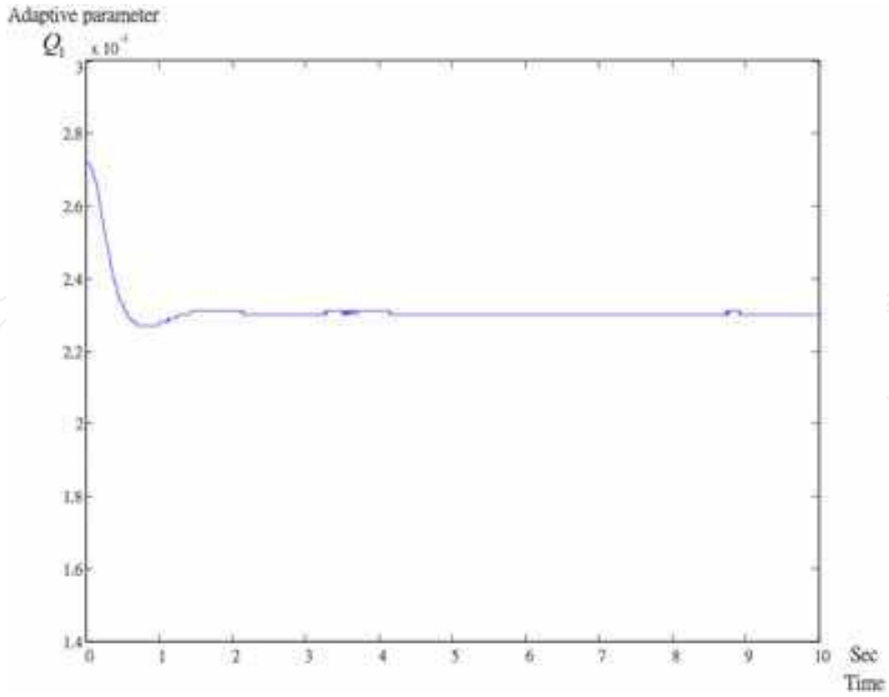
Adaptive parameter
Q1
x 10^-4
3
2.8
2.6
2.4
2.2
2
1.8
1.6
1.4
0 1 2 3 4 5 6 7 8 9 10
Sec
Time

(b)

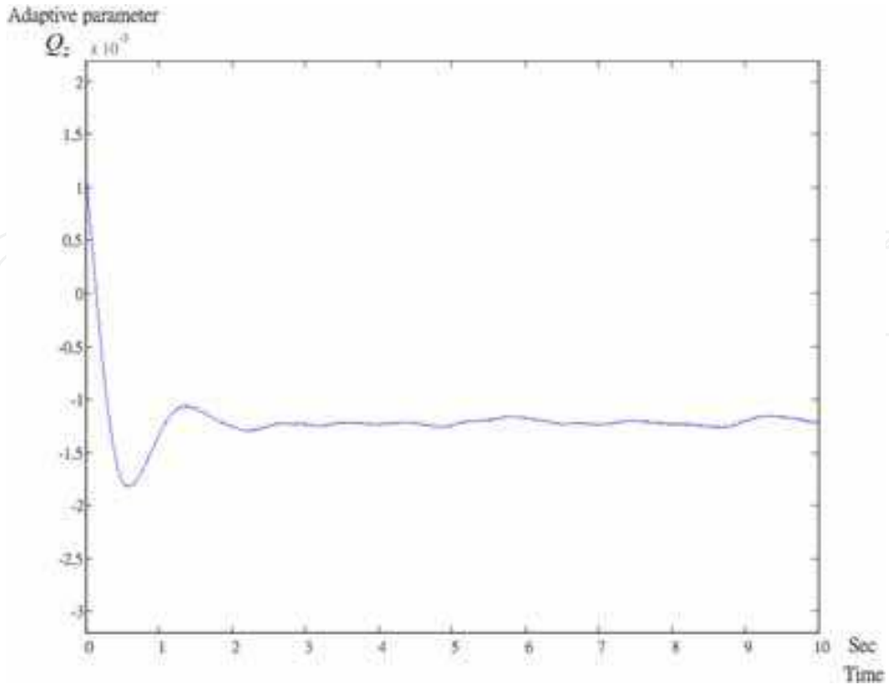

(c)

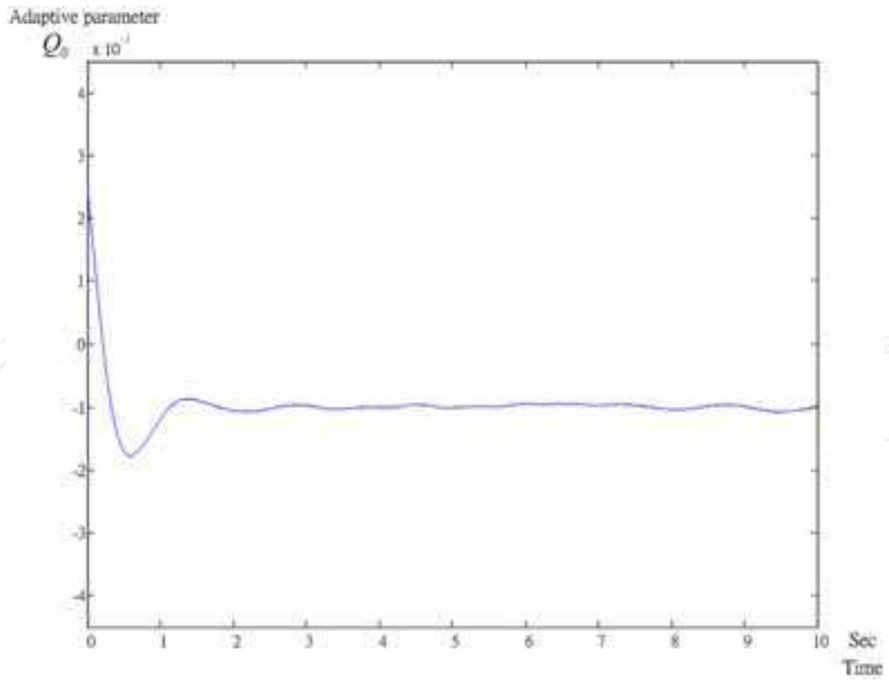

(d)

Fig. 23. The measured responses of model-reference control. (a) K (b) Q_1 (c) Q_2 (d) Q_0 .

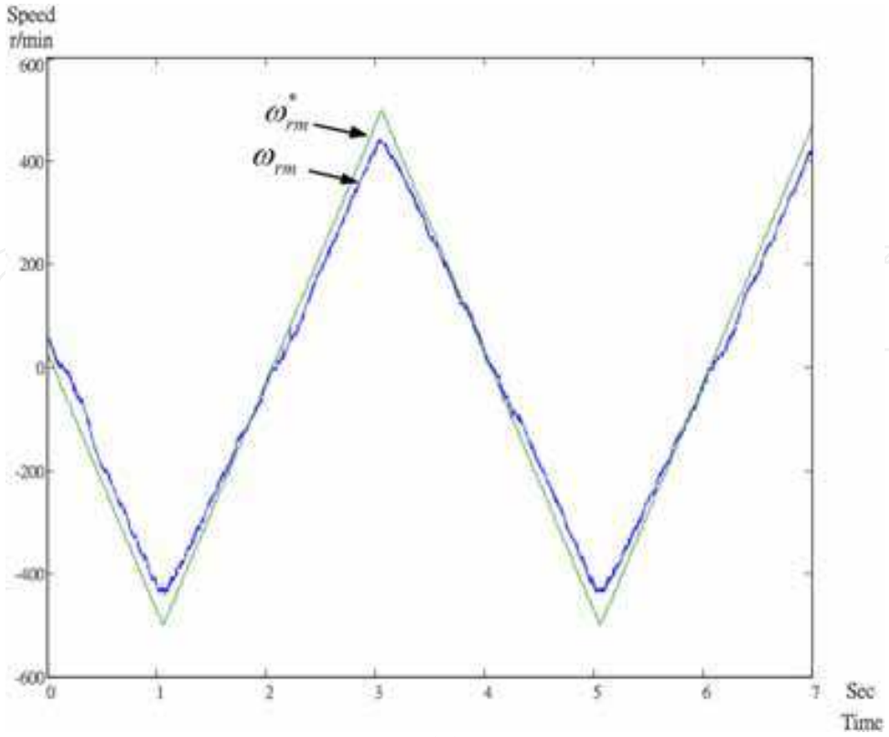
Speed
r/min
600
400
200
0
-200
-400
-600
0
1
2
3
4
5
6
7
Sec
Time
ω_{rm}^*
ω_{rm}

(a)

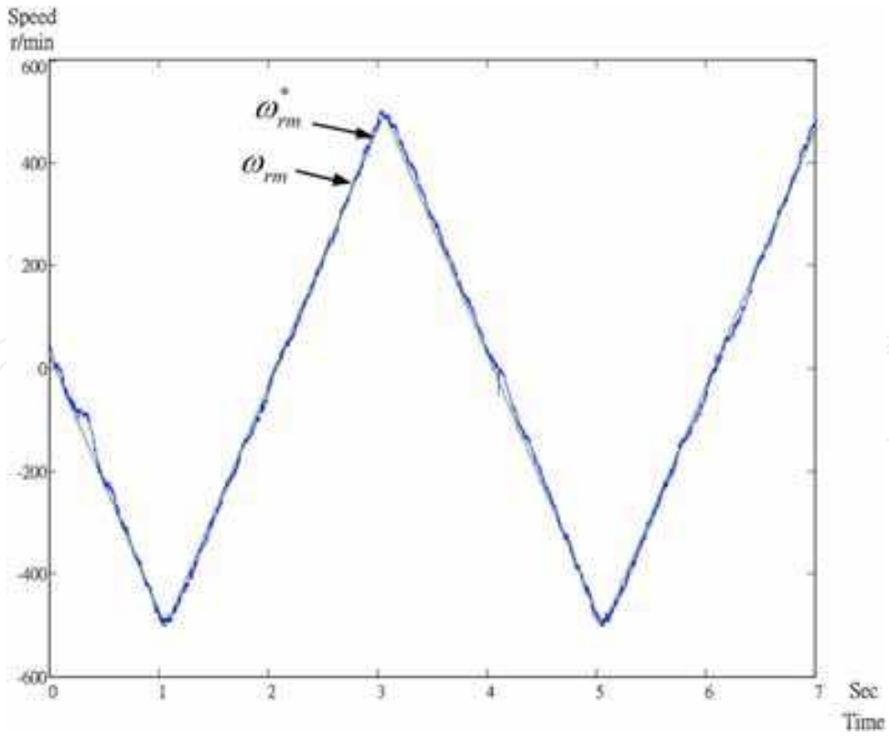
Speed
r/min
600
400
200
0
-200
-400
-600
0
1
2
3
4
5
6
7
Sec
Time
ω_{rm}^*
ω_{rm}

(b)

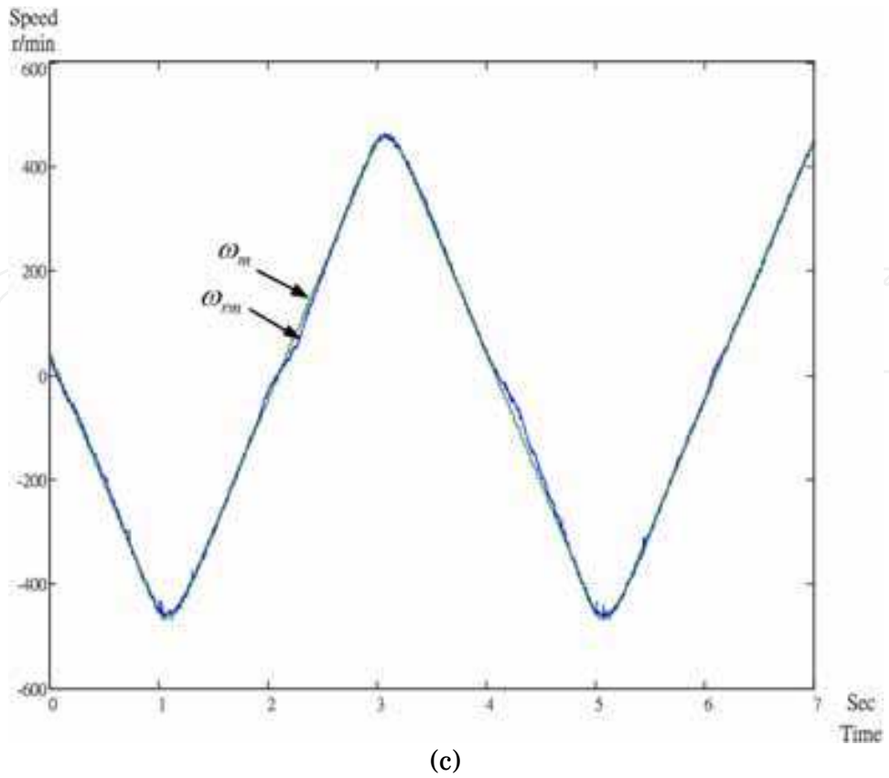

(c)

Fig. 24 The measured speed responses of a triangular speed command.
(a) PI (b) backstepping (c) model-reference.

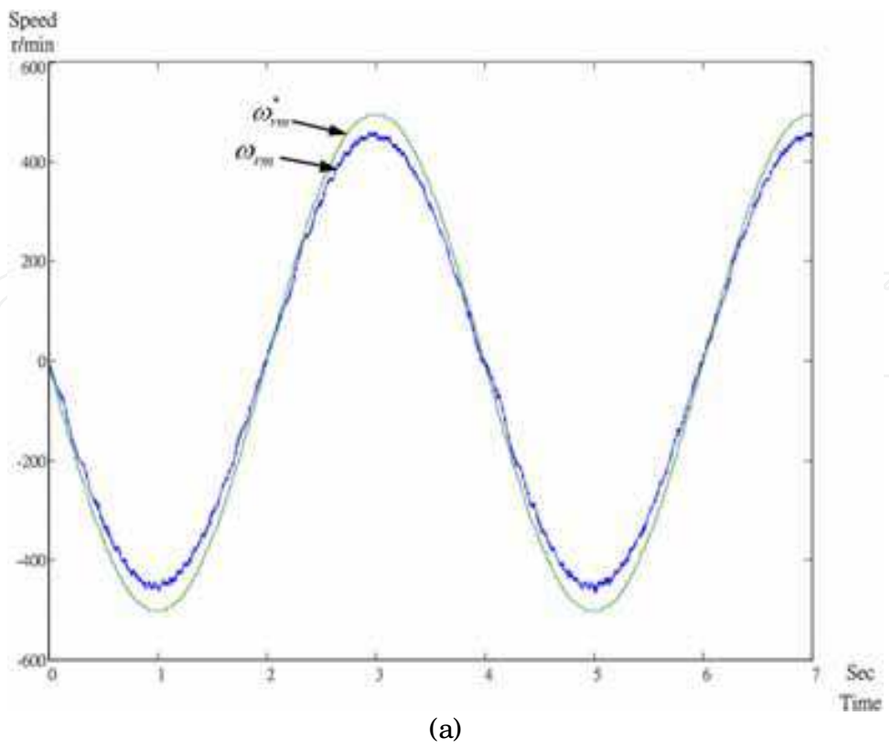

(a)

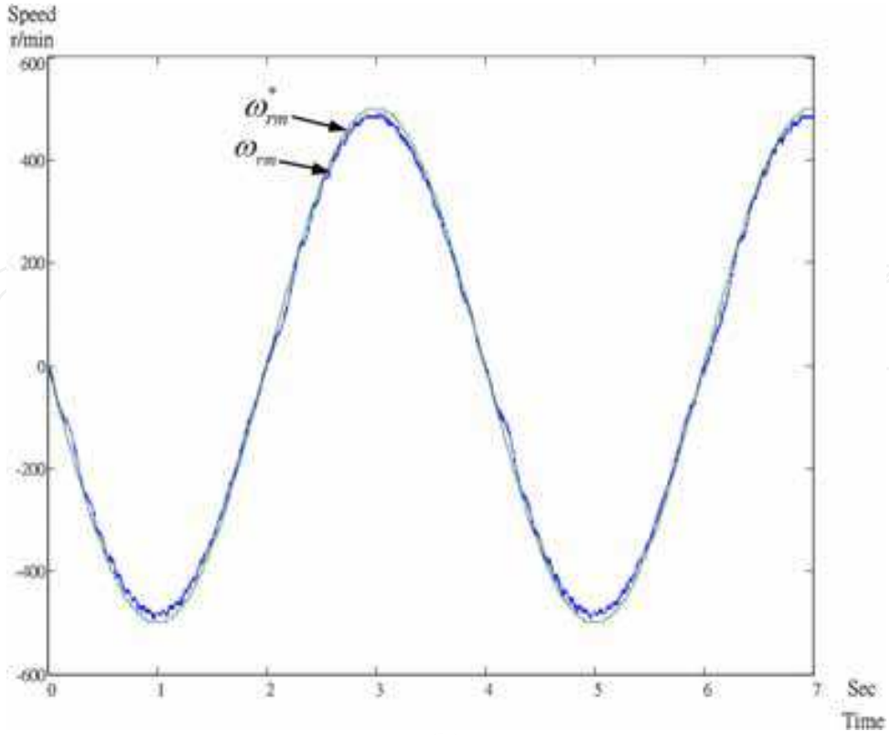

(b)

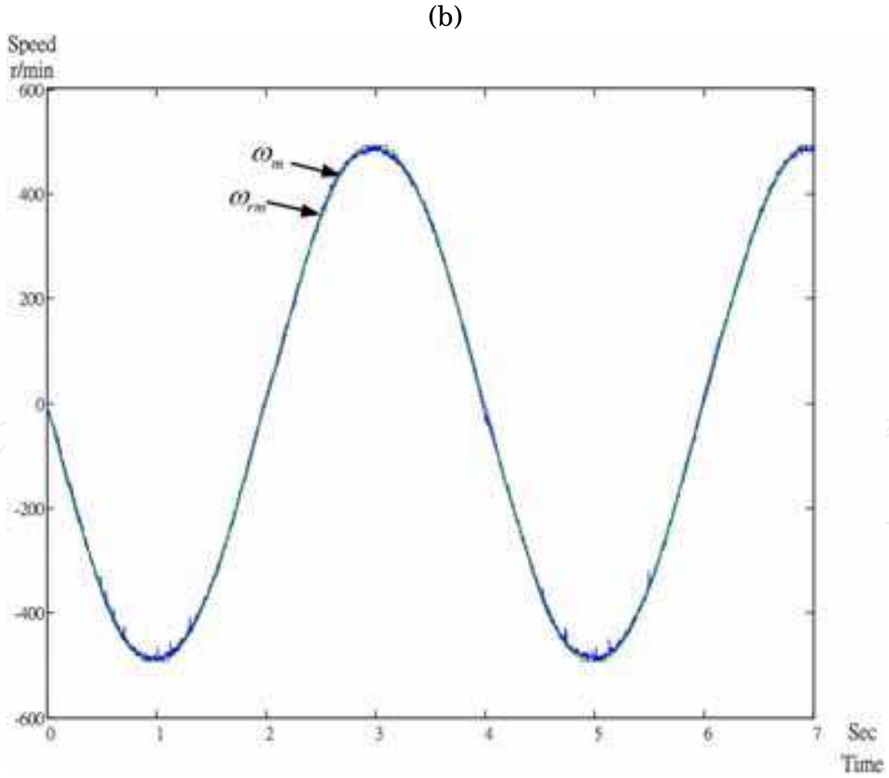

(c)

Fig. 25. The speed responses of a sinusoidal speed command. (a) PI (b) backstepping (c) model-reference.

6. Future trends

In this chapter, by using the torque control, a closed-loop sensorless speed drive system has been implemented. The proposed system can be operated from 30 r/ min to 2000 r/ min with satisfactory performance. Unfortunately, the proposed system cannot be operated from standstill to 30 r/ min. As a result, it is necessary in the future to continuously improve the controller design, hardware design, and software design to reduce the torque pulsations and then provide better performance in low-speed operating range. In addition, it is another aim to realize a closed-loop high performance position control system by using a torque control method.

7. Conclusions

In this chapter, two different adaptive controllers have been proposed for a synchronous reluctance motor drive system. The parameters of the controllers are on-line tuned. The adaptive backstepping controller has simple control algorithm. It is more easily implemented than the model reference adaptive controller is. On the other hand, the model reference adaptive controller performs better in transient responses and steady-state characteristics. A digital signal process is used to execute the control algorithm. As a result, the hardware circuit is very simple. The implemented system shows good transient responses, load disturbance responses, and tracking ability in triangular and sinusoidal commands. This paper provides a new direction in the application of adaptive controller design for a synchronous reluctance motor drive system.

8. References

[1] Park, J. M., Kim, S., Hong, J. P., and Lee, J. H.: 'Rotor design on torque ripple reduction for a synchronous reluctance motor with concentrated winding using response surface methodology', IEEE Trans. Magnet., vol. 42, no. 10, pp. 3479-3481, 2006.

[2] G. Sturtzer, D. Flieller, and J. P. Louis, "Mathematical and experi- mental method to obtain the inverse modeling of nonsinusoidal and saturated synchronous reluctance motors," IEEE Trans. Energy Conversion, vol. 18, no. 4, pp. 494-500, Dec. 2003.

[3] Hofmann, H. F., Sanders, S. R., and Antably, A.: 'Stator-flux-oriented vector control of synchronous reluctance machines with maximized efficiency', IEEE Trans. Ind. Electron., vol. 51, no. 5, pp. 1066-1072, 2004.

[4] M. T. Lin, and T. H. Liu, "Sensorless synchronous reluctance drive with standstill starting," IEEE Aerosp. Electron. Syst. Mag., vol. 36, no. 4, pp. 1232-1241, Oct. 2000.

[5] S. Ichikawa, A. Iwata, M. Tomitat, S. Doki, and S. Okuma, "Sensorless control of synchronous reluctance motors using an on-line parameter identification method taking into account magnetic saturation," IEEE PESC '04, pp. 3311-3316, June 2004.

[6] L. Xu, X. Xu, T. A. Lipo, and D. W. Novotny, "Vector control of a synchronous reluctance motor including saturation and iron loss," IEEE Trans. Ind. Appl., vol. 27, no. 5, pp. 977-985, Sept./ Oct. 1991.

[7] S. Morimoto, M. Sanada, and Y. Takeda, "High-performance current -sensorless drive for PMSM and SynRM with only low-resolution position sensor," IEEE Trans. Ind. Appl., vol. 39, no. 3, pp. 792-801, May/ June 2003.

[8] C. G. Chen, T. H. Liu, M. T. Lin, and C. A. Tai, "Position control of a sensorless synchronous reluctance motor," IEEE Trans. Ind. Appl., vol. 51, no. 1, pp. 15-25, Feb. 2004.

[9] M. G. Jovanovic, R. E. Betz, and D. Platt, "Sensorless vector controller for a synchronous reluctance motor," IEEE Trans. Ind. Appl., vol. 34, no. 2, pp. 346-354, Mar./ Apr. 1998.

[10] S. Ichikawa, M. Tomitat, S. Doki, and S. Okuma, "Sensorless control of synchronous reluctance motors based on an extended EMF model and initial position estimation," IEEE IECON '03, pp. 2150-2155, Nov. 2003.

[11] J. I. Ha, S. J. Kang, and S. K. Sul, "Position controlled synchronous reluctance motor without rotational transducer," IEEE Trans. Ind. Appl., vol. 35, no. 6, pp. 1393-1398, Nov./ Dec. 1999.

[12] Y. Q. Xiang, and S. A. Nasar, "A fully digital control strategy for synchronous reluctance motor servo drives," IEEE Trans. Ind. Appl., vol 33, no. 3, pp. 705-713, May/ June 1997.

[13] D. Telford, M. W. Dunnigan, and B. W. Williams, "A novel torque-ripple reduction strategy for direct torque control," IEEE Trans. Ind. Electron., vol. 48, no. 4, pp. 867-870, Aug. 2001.

[14] J. H. Lee, C. G. Kim, and M. J. Youn, "A dead-beat type digital controller for the direct torque control of an induction motor," IEEE Trans. Power Electron., vol. 17, no. 5, pp. 739-746, Sep. 2002.

[15] J. Beerten, J. Verveckken, and J. Driesen, "Predictive direct torque control for flux and torque ripple reduction," IEEE Trans. Ind. Electron., vol. 57, no. 1, pp. 404-412, Jan. 2010.

[16] Consoli, A., Cavallars, C., Scarcella, G., and Testa, A.: 'Sensorless torque control of synchronous motor drives," IEEE Trans. Pow. Electron., Vol. 15, no. 1, pp. 28-35, 2000.

[17] D. A. Staton, T. J. E. Miller, and S. E. Wood, "Maximising the saliency ratio of the synchronous reluctance motor," IEE Proc. Electr. Power Appl., vol. 140, no. 4, pp. 249-259, July 1993.

[18] A. Vagati, A. Canova, M. Chiampi, M. Pastorelli, and M. Repetto, "Design refinement of synchronous reluctance motors through finite-element analysis," IEEE Trans. Ind. Electron., vol. 36, no. 4, pp. 1094-1102, July/ Aug. 2000.

[19] K. Uezato, T. Senjyu, and Y. Tomori, "Modeling and vector control of synchronous reluctance motors including stator iron loss," IEEE Trans. Ind. Electron., vol. 30, no. 4, pp. 971-976, July/ Aug. 1994.

[20] G. Stumberger, B. Stumberger, and D. Dolinar, "Identification of linear synchronous reluctance motor parameters," IEEE Trans. Ind. Appl., vol. 40, no. 5, pp. 1317-1324, Sept./ Oct. 2004.

[21] H. K. Chiang and C. H. Tseng, "Integral variable structure controller with grey prediction for synchronous reluctance motor drive," IEE Proc. Electr. Power Appl., vol. 151, no. 3, pp. 349-358, May 2004.

[22] C. H. Lin, "Adaptive recurrent fuzzy neural network control for synchronous reluctance motor servo drive," IEE Proc. Electr. Power Appl., vol. 151, no. 6, pp. 711-724, Nov. 2004.

[23] S. J. Kang, J. M. Kim, and S. K. Sul, "Position sensorless control of synchronous reluctance motor using high frequency current injection," IEEE Trans. Energy Conversion, vol. 14, no. 4, pp. 1271-1275, Dec. 1999.

[24] R. Shi, and H. A. Toliyat, "Vector control of five-phase synchronous reluctance motor with space vector pulse width modulation (SVPWM) for minimum switching losses," IEEE APEC '02, pp. 57-63, Mar. 2002.

[25] Y. Gao and K. T. Chau, "Hopf bifurcation and chaos in synchronous reluctance motor drives," IEEE Trans. Energy Conversion, vol. 19, no. 2, pp. 296-302, June 2004.

[26] N. Bianchi, S. Bolognani, D. Bon, and M. D. Pre, "Torque harmonic compensation in a synchronous reluctance motor," IEEE Trans. Energy Conversion, vol. 23, no. 2, pp. 466-473, June 2008.

[27] A. Iqbal, "Dynamic performance of a vector-controlled five-phase synchronous reluctance motor drive: an experimental investigation," IET Electr. Power Appl., vol. 2, no. 5, pp. 298-305, 2008.

[28] R. Morales-Caporal and M. Pacas, "Encoderless predictive direct torque control for synchronous reluctance machines at very low and zero speed," IEEE Trans. Ind. Electron., vol. 55, no. 12, pp. 4408-4416, Dec. 2008.

[29] J. D. Park, C. Kalev, and H. F. Hofmann, "Control of high-speed solid-rotor synchronous reluctance motor/ generator for flywheel-based uninterruptible power supplies," IEEE Trans. Ind. Electron., vol. 55, no. 8, pp. 3038-3046, Aug. 2008.

[30] T. H. Liu, M. T. Lin, and Y. C. Yang, "Nonlinear control of a synchronous reluctance drive system with reduced switching frequency," IEE Electr. Power Appl., vol. 153, no. 1, pp. 47-56, Jan. 2006.

[31] S. Ichikawa, M. Tomita, S. Doki, and S. Okuma, "Sensorless control of synchronous reluctance motors based on extended EMF models considering magnetic saturation with online parameter identification," IEEE Trans. Ind. Appl., vol. 42, no. 5, pp. 1264-1274, Sep./ Oct. 2006.

[32] Kristic, M., Kanellakopoulos, I., and Kokotovic, P. V. : 'Nonlinear and Adaptive Control Design, (New York: John Wiley and Sons Inc, 1995).

[33] Narendra, K. S. and Annaswamy, A. M. : Stable Adaptive Systems, (New Jersey: Prentice-Hall, 1989).

[34] Tao, G.: Adaptive Control Design and Analysis, (New Jersey: Wiley-Interscience, 2003).

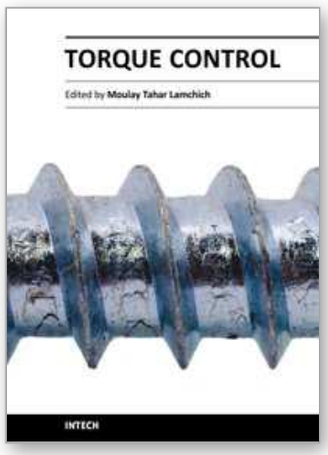

Torque Control

Edited by Prof. Moulay Tahar Lamchich

ISBN 978-953-307-428-3
Hard cover, 292 pages
Publisher InTech
Published online 10, February, 2011
Published in print edition February, 2011

This book is the result of inspirations and contributions from many researchers, a collection of 9 works, which are, in majority, focalised around the Direct Torque Control and may be comprised of three sections: different techniques for the control of asynchronous motors and double feed or double star induction machines, oriented approach of recent developments relating to the control of the Permanent Magnet Synchronous Motors, and special controller design and torque control of switched reluctance machine.

How to reference

In order to correctly reference this scholarly work, feel free to copy and paste the following:

Tian-Hua Liu (2011). Controller Design for Synchronous Reluctance Motor Drive Systems with Direct Torque Control, Torque Control, Prof. Moulay Tahar Lamchich (Ed.), ISBN: 978-953-307-428-3, InTech, Available from: http://www.intechopen.com/books/torque-control/controller-design-for-synchronous-reluctance-motor-drive-systems-with-direct-torque-control

INTECH
open science | open minds

InTech Europe
University Campus STeP Ri
Slavka Krautzeka 83/A
51000 Rijeka, Croatia
Phone: +385 (51) 770 447
Fax: +385 (51) 686 166
www.intechopen.com

InTech China
Unit 405, Office Block, Hotel Equatorial Shanghai
No.65, Yan An Road (West), Shanghai, 200040, China
中国上海市延安西路65号上海国际贵都大饭店办公楼405单元
Phone: +86-21-62489820
Fax: +86-21-62489821

IntechOpen